Assignment of spin and parity to states in the nucleus ^{196}Tl

Pierre Celestin Uwitonze

Supervisor: Dr. David Roux

Department of Physics

Rhodes University

A dissertation submitted to the Physics Department in fulfilment of the Degree of Master of Science

September 17, 2014

Abstract

This work presents a study of high-spin states in the nucleus ^{196}Tl via γ-spectroscopy. ^{196}Tl was produced via the ^{197}Au(^{4}He,5n)^{196}Tl reaction at a beam energy of 63 MeV. The $\gamma - \gamma$ coincidence measurements were performed using the AFRODITE γ-spectrometer array at iThemba LABS. The previous level scheme of ^{196}Tl has been extended up to an excitation energy of 4071 keV including 24 new γ-ray transitions. The spin and parity assignment to levels was made from the directional correlation of oriented nuclei (DCO) and linear polarization anisotropy ratios. An analysis of the $B(M1)/B(E2)$ ratios was found to be consistent with the configuration of $\pi h_{9/2} \otimes \nu i_{13/2}$ for the ground state band. Although no chiral band was found in ^{196}Tl, such band have been found in neighboring nuclei ^{194}Tl and ^{198}Tl.

Contents

Chapter 1

INTRODUCTION

The thallium nuclei, with proton number $Z = 81$, are situated in a transition region between the deformed prolate rare-earth nuclei and the spherical lead nuclei at $Z = 82$. The proton Fermi level lies near the $3s_{1/2}$ orbital and the ground-state spin-parity of odd-A Tl isotopes in the $A \sim 190$ region, is accordingly $1/2^+$. Also the intruder $[505]9/2^-$ and $[541]1/2^-$ Nilsson states originating from the $\pi h_{9/2}$ orbital above $Z = 82$ are available near the Fermi surface for oblate and prolate deformation respectively [1]. Strongly coupled bands built on the $9/2^-$ state were observed in odd-A Tl isotopes [1–3]. The neutron Fermi level for the Tl and Hg isotopes in the $A \sim 190$ region lies near the top of the $1i_{13/2}$ orbital and decoupled bands with this configuration were observed in odd-A Hg isotopes in this region [4–6]. Therefore, for odd-odd Tl isotopes in the $A \sim 190$ region, rotational bands based on the $\pi h_{9/2} \otimes \nu i_{13/2}$ configuration are expected. Many works on odd-odd Tl isotopes in $190 \leq A \leq 200$ region showed that the yrast bands in these nuclei are associated with the $\pi h_{9/2} \otimes \nu i_{13/2}$ configuration and that they are oblate [1–3, 7–14]. However, a possible chiral band was found in ^{198}Tl [15] and recently suggested in ^{194}Tl [16] which indicated a non-axial deformation. It is most likely that such a band can be observed in other odd-odd Tl nuclei including ^{196}Tl as the yrast bands of these nuclei share very similar properties [8–10]. This is the reason why we were interested to investigate the

configuration of the yrast band in the ^{196}Tl nucleus, and search for a possible chiral band in this nucleus.

High spin states in ^{196}Tl were studied by Kreiner *et al.* [7] in early 1978 using Ge(Li) detectors. The level scheme presented in that work is shown in Fig. 5.1. It consists of three bands of transitions in cascades and only the strong yrast band was assigned tentative spin and parity. This band was studied using the particle-plus-rotor model [11] and was interpreted to be a $\pi h_{9/2} \otimes \nu i_{13/2}$ band with an oblate deformation. In the present work, high-spin states in ^{196}Tl were studied using high purity germanium (HPGe) detectors and thus an improved level scheme was expected. We hoped also to assign spin and parity to Bands 2 and 3 for the first time. The interpretation of rotational bands in terms of the Cranked Shell Model (CSM) and Total Routhian Surface calculations (TRS) could allow us to search for a possible chirality in this nucleus.

This thesis is organised as follows: Chapter 2 describes briefly the theory of γ-radiation and rotational bands. Chapter 3 details the experimental tools and techniques used in γ-spectroscopy. Chapter 4 describes the experiment and the sorting of raw data into analysable data. Chapter 5, which is the main part of this thesis, presents the results of the analysis and discusses the assignment of spin and parity to new levels. Chapter 6 presents the interpretation of Band 1 in terms of the CSM and TRS. The reduced transition probability $B(E2)/(M1)$ is used to assign the configuration to Band 1 of ^{196}Tl.

Chapter 2

THEORY

2.1 Nuclear deformation and its parameters

The spherical shell model [17] does not adequately describe the nuclei far from closed shells. For these regions a deformed potential has to be assumed. The assumption of a deformation is able to explain some experimental facts such as rotational bands and very large quadrupole moments.

The nuclear surface of a non-spherical nucleus is described by [17]:

$$R(\theta,\phi) = R_0(1 + \sum_{\lambda=2}^{\infty}\sum_{\mu=0}^{\lambda}\alpha_{\lambda\mu}Y_{\lambda\mu}(\theta,\phi)) \ , \tag{2.1}$$

where $\alpha_{\lambda\mu}$ are the expansion coefficients for the spherical harmonics $Y_{\lambda\mu}(\theta,\phi)$ and R_0 is the average nuclear radius.

For axial quadrupole-deformed nuclei, the radius is defined as:

$$R(\theta) = R_0(1 + \beta_2 Y_{20}(\theta)) \ , \tag{2.2}$$

where the deformation parameter $\beta_2 = \alpha_{20}$. If $\beta_2 < 0$ the nuclear shape is *oblate* (flattened sphere), if $\beta_2 > 0$ the nuclear shape is *prolate* like a rugby ball, and if $\beta_2 = 0$ then

the nucleus is spherical. The larger the value of β_2, the more deformed nucleus.

Nuclei having a shape of three principal axes with different lengths, are described as *axially asymmetric* and a new deformation parameter γ enters into the description of their nuclear shape which is related to the $\alpha_{\lambda\mu}$ coefficient as follows [17]:

$$\alpha_{20} = \beta_2 \cos\gamma \ , \tag{2.3}$$

$$\alpha_{22} = \frac{1}{\sqrt{2}}\beta_2 \sin\gamma \cdot \tag{2.4}$$

The γ deformation ranges from -120° to 60° corresponding to non-collective prolate and non-collective oblate shapes respectively [18]. $\gamma = 0°$ corresponds to a collective prolate shape and γ = -60° to a collective oblate shape. A nucleus has maximum triaxial deformation when $\gamma \pm 30°$ [18].

2.2 Nilsson shell model

The Nilsson model uses a deformed harmonic oscillator potential to predict the effect of core deformation on the relative energies of the single-particle levels [19]. In this model, the Schrödinger equation is solved with a deformed harmonic oscillator potential that is parametrised with the deformation parameter β_2. The single-particle energy levels are given by the Nilsson diagrams for neutrons and protons separately. As an example, the Nilsson single-particle energy level diagrams for neutrons in the $82 \leq N \leq 126$ region and proton in $80 \leq Z \leq 120$ region are given in Figures 2.1 and 2.2 respectively as function of deformation parameters. Here the deformation parameter ϵ_2 is used and is related to β_2 as $\epsilon_2 \simeq 0.95\beta_2$ [20].

It can be seen that at zero deformation, states with the same j are degenerate and when the deformation is introduced, the different magnetic substates undergo a splitting

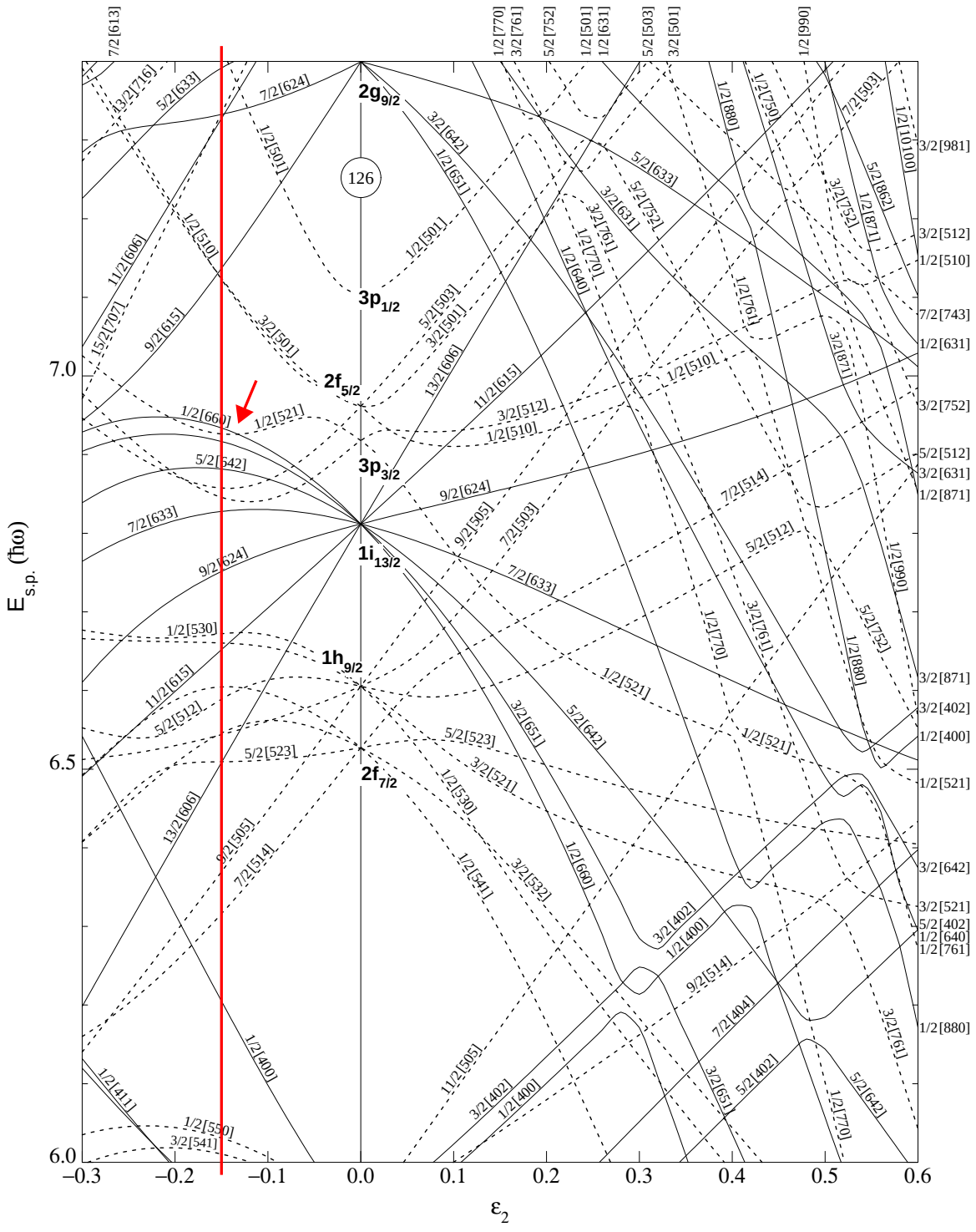

Figure 2.1: Nilsson diagram for neutrons, $82 \leq N \leq 126$ as a function of deformation ε_2. The solid lines correspond to positive parity orbitals and the dashed lines correspond to negative orbitals [19]. The arrow shows the position of the neutron Fermi surface for ^{196}Tl.

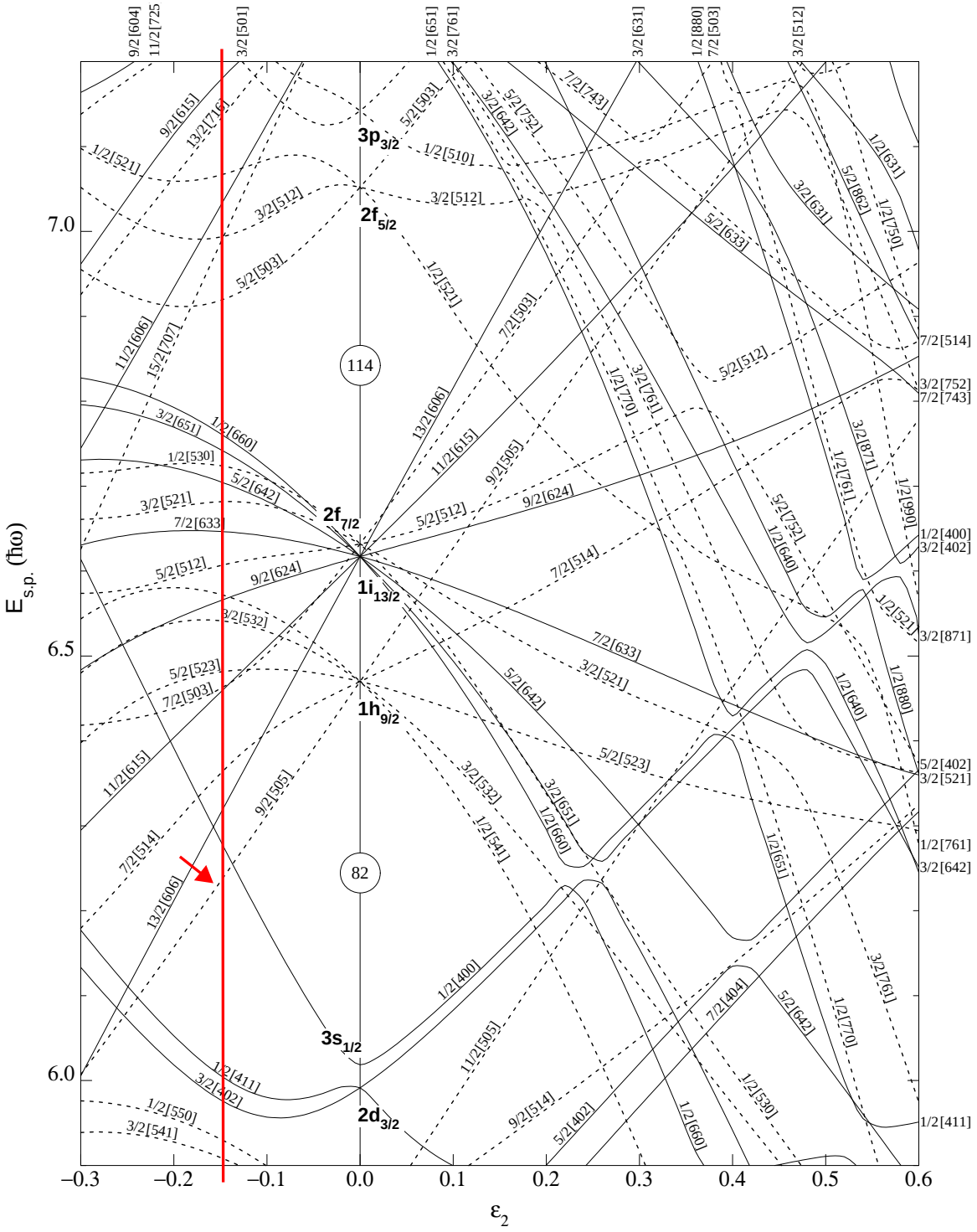

Figure 2.2: Nilsson diagram of single-particle levels for protons $Z \geq 82$ as a function of deformation ε_2. The solid lines correspond to positive parity orbitals and the dashed lines correspond to negative orbitals [19]. The arrow shows the position of the proton Fermi surface for ^{196}Tl.

in energy. The upward or downward sloping of the orbital energies depends on whether the nuclear deformation is prolate or oblate.

The Nilsson orbitals are characterized by the quantum numbers:

$$[Nn_z\Lambda]\Omega^\pi \ , \tag{2.5}$$

where Ω is the projection of the angular momentum onto the symmetry axis, and N is the principal quantum number of the major shell and determines the parity π. n_z is the number of nodes of the wave function along the direction of the symmetry axis and Λ is the projection of the orbital angular momentum onto the symmetry axis such that $\Omega = \Lambda \pm 1/2$. For example in ^{196}Tl nucleus the neutron and proton Fermi surfaces are close to the $[660]1/2^+$ and $[505]9/2^-$ Nilsson orbitals respectively for oblate deformation. These levels are indicated with an arrow in the Figure 2.1 and 2.2 respectively.

2.3 Nuclear rotation

Nuclear rotation is a mode of excitation observed only in deformed nuclei [15] where the nucleus rotates around an axis (usually called the x-axis) perpendicular to the axis of symmetry (usually called the z-axis). For the case of odd-A nuclei, a model that describes the spectra well is the Particle Rotor Model (PRM), in which one or more unpaired nucleons are viewed as being coupled to the even-even core. In this mode, the collective motion of the core generates the rotational angular momentum $\vec{R}$ and the unpaired nucleon outside the core generates the additional angular momentum $\vec{j}$. The two angular momenta couple to give the total angular momentum $\vec{I}$ such that

$$\vec{I} = \vec{R} + \vec{j} \cdot \tag{2.6}$$

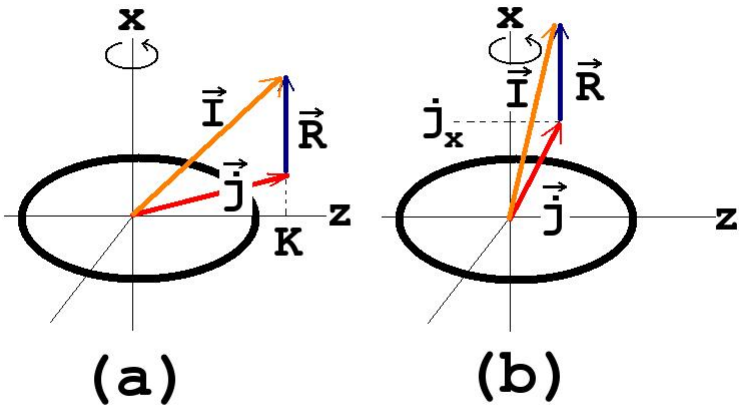

Figure 2.3: Panel (a) shows the deformation aligned coupling scheme (DAL), where the angular momentum $\vec{I}$ has the maximum projection K along the symmetry axis. Panel (b) shows the rotation aligned coupling scheme (RAL), where the angular momentum $\vec{j}$ has the maximum projection j_x along the rotation axis. $\vec{R}$ is the collective angular momentum and $\vec{j}$ is a single particle angular momentum.

The rotational motion of the nucleus shows a series of excited levels known as a *rotational band*. In the following we discuss three types of rotational band.

Deformation aligned bands (DAL)

DAL bands are also called *strongly coupled bands* because the vector $\vec{I}$ rotates in step with the core so it is coupled to the collective rotation. These bands reflect the rotation of a nucleus with one or more odd nucleons [21]. The projection of $\vec{j}$ on the symmetry axis is a good quantum number K ($K = \sum \Omega_i$) (see Figure 2.3 (a)). The resulting band consists of a series of levels with spins $I = K$, $K+1$, $K+2$, $K+3$, etc, and the energy of the levels is given by:

$$E(I) = \frac{\hbar^2}{2\mathscr{I}_0}[I(I+1) - K(K+1)] \tag{2.7}$$

when $K \neq 1/2$ and

$$E(I) = \frac{\hbar^2}{2\mathscr{I}_0}[I(I+1) + (-1)^{I+1/2}(I+1/2)] \tag{2.8}$$

when $K = 1/2$. The $\mathscr{I}_0$ is the moment of inertia and depends on the shape and the internal structure of the nucleus. The excited levels of the band decay via M1 and E2 transitions to the ground state level.

Rotation aligned bands (RAL)

For RAL bands also called *decoupled bands*, the angular momentum $\vec{I}$ has the maximum projection along the rotation axis (see Figure 2.3 (b)). The projection of odd particle angular momentum $\vec{j}$ along the rotation axis is a good quantum number j_x. The resulting band consists of a series of levels with spins $I = j_x$, j_x+2, j_x+4, etc, and the energy relative to the band level with spin $I = j_x$ is given by:

$$E(I) = \frac{\hbar^2}{2\mathscr{I}_0}[(I - j_x)(I - j_x + 1)] \cdot \tag{2.9}$$

These levels decay to the ground state through stretched $E2$ transitions. Here the transition is called *stretched* when the multipolarity λ of γ-ray equals the spin difference between the initial and final states. eg. $E2$ connecting states of $I + 2$ and I is a stretched $E2$ transition.

Rotational bands of even-even nuclei

For even-even nuclei, all the nucleons are paired and the nucleus rotates as a whole around the rotational axis.

The excitation energy of these levels is given by:

$$E(I) = \frac{\hbar^2}{2\mathscr{I}_0} I(I + 1) \ , \tag{2.10}$$

The ground state band thus consists of a sequence of levels with even spins of 0^+, 2^+, 4^+, 6^+ etc, which decay through stretched $E2$ transitions to the ground state 0^+. In particular the energy ratio $E(4^+)/E(2^+) = 3.3$ characterises the rotational bands of

even-even nuclei.

2.4 Cranked Shell Model

Among theoretical models aiming at the description of high-spin states, the Cranked Shell Model (CSM) is one of the most successful because it describes a nucleus with stable deformation and pairing interactions, which is rotating. It combines in the same formalism the description of collective rotational bands and excited particle configurations, which are the two most important types of excitation at high spins [21].

Cranking Hamiltonian

In the CSM, the rotation is treated classically and the nucleons are considered as independent particles moving in an average potential which is rotating with a constant angular velocity ω. Here, the intrinsic coordinate system (x_1, x_2, x_3) rotates with the rotational frequency ω, relative to the laboratory coordinate system (x, y, z). If the axis of rotation is the x-axis, this coincides with the x_1-axis which is perpendicular to the system axis x_3. The total cranking Hamiltonian for a system of A nucleons is given by [22]:

$$H^{\omega} = H^0 - \hbar\omega I_x = \sum_{\mu=1}^{A} h_{\mu}^0 - \hbar\omega j_{x\mu} = \sum_{\mu=1}^{A} h_{\mu}^{\omega} \,, \tag{2.11}$$

where H^{ω} is the total Hamiltonian in the rotating frame, H^0 is the total Hamiltonian in the laboratory system and I_x is the total angular momentum projection onto the rotation axis. $h_{\mu}^{\omega} = h_{\mu}^0 - \hbar\omega j_{x\mu}$ is the single particle Hamiltonian in the rotating frame, h_{μ}^0 is the single particle Hamiltonian in the laboratory system and $j_{x\mu}$ is the single particle angular momentum projection onto the rotation axis.

The $-\hbar\omega j_{x\mu}$ term contains the Coriolis force which tends to align the angular momentum of the nucleons with the rotation axis. The eigenvalues of the Hamiltonian (H^{ω}) are known as *Routhians* (the single-particle energies in the rotating frame) and are equal

to [22]:

$$E^{\omega} = \sum_{\mu=1}^{A} e_{\mu}^{\omega} = E - \hbar\omega \sum_{\mu=1}^{A} \langle \mu^{\omega} | j_{x\mu} | \mu^{\omega} \rangle \ , \tag{2.12}$$

where E^{ω} denotes the total Routhian, e_{μ}^{ω} denotes the single-particle Routhian, E is the total energy in the laboratory frame, and $|\mu^{\omega}\rangle$ are the single particle eigenfunctions in the rotating frame. The projection of the total angular momentum onto the rotation axis can be written as

$$I_x = \sum_{\mu=1}^{A} \langle \mu^{\omega} | j_{x\mu} | \mu^{\omega} \rangle \cdot \tag{2.13}$$

The slope of the Routhian is related to the alignment, i_x defined as

$$i_x = -\frac{de_{\mu}^{\omega}}{d\omega} \cdot \tag{2.14}$$

In the CSM, the Nilsson quantum number Ω is no longer good because the $-\omega j_x$ term in the cranking Hamiltonian breaks the time-reversal symmetry [23].

Symmetries and quantum numbers in CSM

In the CSM there are only two symmetries of the Hamiltonian and these are related to the two remaining good quantum numbers, π and α. The parity (π) describes the symmetry of the Hamiltonian under space reflection, and the signature (α) describes the symmetry of the nuclear wave function under a rotation of 180° about the rotation axis. For systems with an even number of nucleons, $\alpha = 0$ or 1. $\alpha = 0$ corresponds to even values of I and $\alpha = 1$ corresponds to odd values of I. For odd A nuclei $\alpha = \pm\ 1/2$. The states with spins $I = 1/2,\ 5/2,\ 9/2,\ 13/2 \cdots$, correspond to $\alpha = +1/2$ and states with $I = 3/2,\ 7/2,\ 11/2,\ 15/2 \cdots$, correspond to $\alpha =$ -1/2. The wave functions of the cranked Hamiltonian are labelled by four combinations of the quantum numbers (π, α,): (+, +1/2), (+, -1/2), (-, +1/2), and (-, -1/2).

When pairing is introduced into the CSM, nuclear excitations are best described in

terms of quasiparticles, which are superpositions of particles and holes. The functions are then the eigenfunctions of the Hartree-Fock-Bogolyubov Hamiltonian which is described in ref. [20, 21]. The quasiparticle eigenvalue problem is given by:

$$H^{\omega}\psi_{\alpha} = E^{\omega}\psi_{\alpha} \tag{2.15}$$

where ψ_{ω} is the eigenfunction corresponding to a quasiparticle state with signature α. The quasiparticle states are classified with respect to (π, α) with the following notations:

$$(\pi,\, \alpha) = (+,\, +1/2) \rightarrow A,\, C,\, \cdots$$
$$(\pi,\, \alpha) = (+,\, \text{-}1/2) \rightarrow B,\, D,\, \cdots$$
$$(\pi,\, \alpha) = (\text{-},\, +1/2) \rightarrow F,\, H,\, \cdots$$
$$(\pi,\, \alpha) = (\text{-},\, \text{-}1/2) \rightarrow E,\, G,\, \cdots$$

where A corresponds to the lowest lying Routhian with (π, α) = (+, +1/2), C to the second lowest one with (π, α) = (+, +1/2), etc.

For example the lowest-lying neutron Routhians in ^{194}Hg [21] are A, B, C, D, E and F originating pair wise from the [660]1/2^{+}, [651]3/2^{+}, [521]1/2^{-} Nilsson levels, and the lowest-lying proton Routhians are e and f originating from the [550]1/2^{-} Nilsson level. The behaviour of these Routhians with rotating frequency is shown in Figure 2.4. From the theoretical point of view, one expects a band-crossing of AB at 0.19 MeV, BC at 0.24 MeV, etc. The band-crossing is associated with the interaction of the occupied Routhians with the unoccupied Routhians with the same parity and signature at a particular frequency ω. It corresponds to the change of the internal structure from that of the ground band to that of the excited band with significant alignment [21].

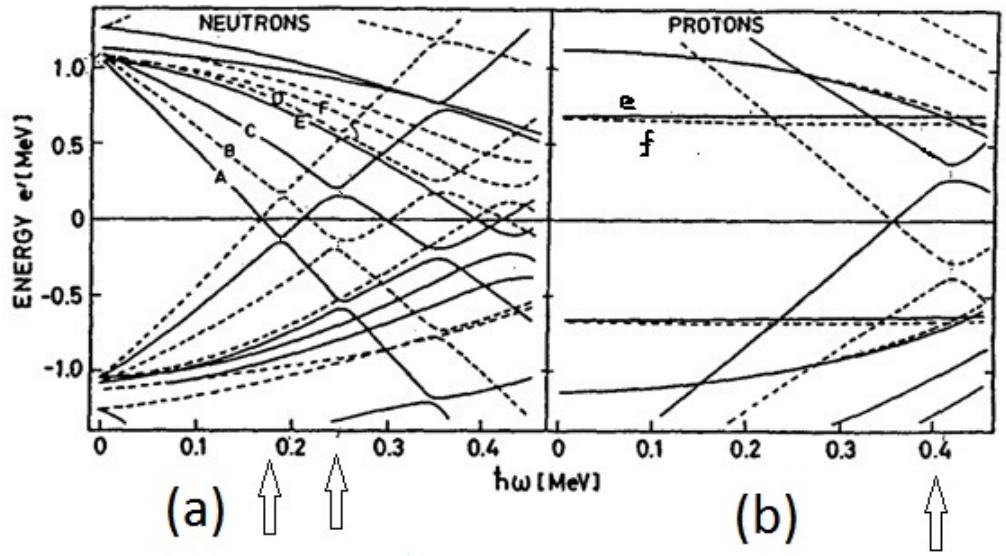

Figure 2.4: Panel (a) ((b)) shows the neutrons (proton) quasiparticle energy levels as function of the rotational frequency for ^{194}Hg. Solid and dashed curves represent states with signatures $\alpha = +1/2$ and $\alpha =$ -1/2 respectively. The arrows indicate the Routhian-crossings AB, BC and ef respectively [21].

2.5 Total Routhian Surface (TRS) calculations

The TRS calculations predict the total Routhian $E^{\omega}(Z, N, \hat{\beta})$ using a shell correction procedure for a given nuclear configuration, a given rotational frequency and as a function of the nuclear deformation [24]. The total Routhian $E^{\omega}(Z, N, \hat{\beta})$ of a nucleus (Z, N) as a function of deformation can be obtained from the sum of the liquid-drop energy, shell correction energy and the pairing correction energy within the cranked Wood-Saxon-Bogolyubov-Strutinsky approach as described in [25]

$$E^{\omega}(Z, N, \hat{\beta}) = E^{\omega}_{LD}(Z, N, \hat{\beta}) + E^{\omega}_{shell}(Z, N, \hat{\beta}) + E^{\omega}_{pair}(Z, N, \hat{\beta}) \ . \tag{2.16}$$

Here $\hat{\beta}$ denotes the complete set of deformation parameters. Usually the TRS plots are calculated using the Hartee-Fock-Bogolyubov code of Nazarewicz *et al.* as explained in [26]. In such plots, the minimum of the contours gives the ground state deformation of the nucleus in terms of β and γ. The $\gamma = 0°$ corresponds to a prolate shape and $\gamma =$ -60° to an oblate shape. As an example, the TRS for the 2-quasiparticle $\pi h_{9/2} \otimes \nu i_{13/2}$ configuration of Band 1 in ^{196}Tl were calculated by Pai *et al.* [1] and the plots are shown in Figure 2.5. The figure clearly shows a minimum in the TRS at a deformation of $\beta \sim$ 0.15 and $\gamma \sim$ -57°, indicating that Band 1 of ^{196}Tl corresponds to an oblate shape.

2.6 Nuclear chirality

The nucleus is said to be chiral if its image in a plane mirror, in the angular momentum space, can not be brought to coincide with itself [27]. Figure 2.6 illustrates a triaxial nucleus having three mutually perpendicular principal axes, short (1), intermediate (2) and long (3). The angular momentum vector of the high-j proton particle, $\vec{j}_{\pi}$ aligns its angular momentum along the short axis (1), the high-j neutron hole aligns its angular momentum $\vec{j}_{\nu}$ along the long axis (3), and the core rotational angular momentum vector,

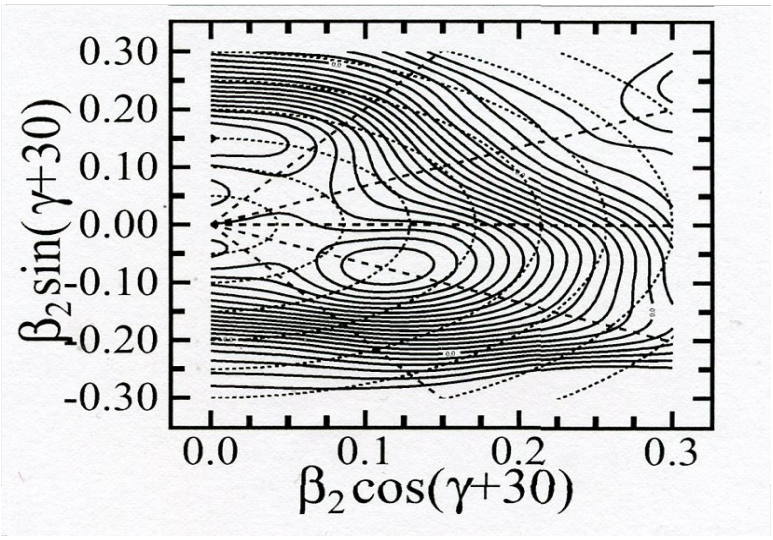

Figure 2.5: Total Routhian surfaces calculated for the $\pi h_{9/2} \otimes \nu i_{13/2}$ configuration of Band 1 in ^{196}Tl [1].

$\vec{R}$ tends to align its angular momentum along the intermediate axis (2). These three mutually perpendicular angular momenta can be arranged in the body-fixed frame to form two systems of opposite handedness, namely, a left-handed or a right-handed system depending upon the direction of the core rotational angular momentum vector. The total angular momentum $\vec{I}$ which does not lie in any of the three principal planes, chooses one of the two systems left-handed or right-handed, thus introducing chirality [28].

Nuclear chirality is expected to be associated with near degenerate bands called chiral

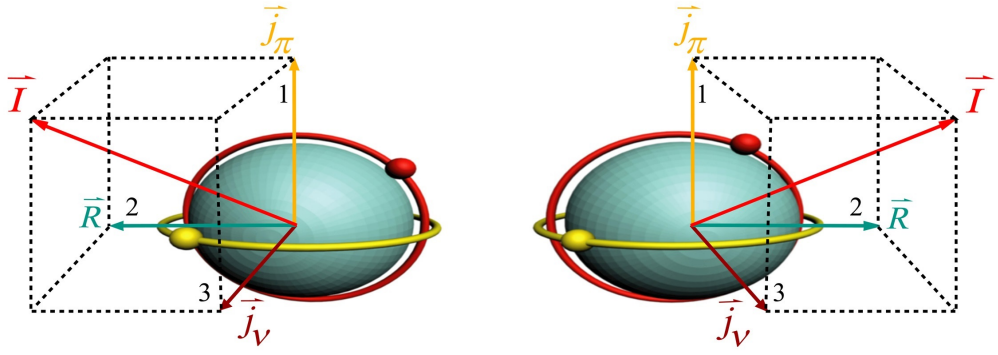

Figure 2.6: Schematic illustration of a chiral system with a left-handed and a right-handed system. Note the orientations of $\vec{R}$ and $\vec{I}$ in the two systems [28].

doublet bands which are commonly connected by several $\Delta I = 1$, $M1/E2$ transitions [27]. For doublet bands to qualify as chiral partners, all their properties should be nearly identical. These are: excitation energy, spin, parity and reduced transition probabilities $B(M1)$ and $B(E2)$. The two bands should be based on the same single-particle configuration, with very similar quasiparticle alignments, moments of inertia and electromagnetic properties.

However a recent work has shown that even the best chiral systems could exhibit divergence in the excitation energies, alignments, the moment of inertia and the $B(M1)$ and $B(E2)$ reduced transition probabilities [28].

A large number of nuclei candidates for chirality were suggested in the mass regions $A \sim 100$, $A \sim 130$ and $A \sim 190$ [1–8, 10–15] but no true degeneracy has been found thus far. This leaves the question whether chiral symmetry exists in nuclei without a clear answer. The occurrence of chirality in nuclei will provide a unique test for the existence of stable triaxial nuclear shapes at moderate spins [29].

2.7 Fusion-evaporation reactions

Fusion evaporation reactions are the most important way of populating high spin states. In this type of reaction, the projectile fuses with the target nucleus to produce a highly excited compound system with high angular momentum. A schematic representation of a fusion-evaporation reaction is shown in Figure 2.7.

For a fusion reaction to occur, the projectile must have enough energy to overcome the Coulomb barrier that exists between the projectile and target nuclei. The compound system obtains its excitation energy from the kinetic energy of collision in the center of mass frame and the reaction Q value. The highly excited compound nucleus thus formed is unstable and needs to get rid of its high excitation energy in one way or another. The product may lose its excitation energy through nuclear fission. The fission process is mostly favoured by the heavy nuclei. The product compound nucleus may also lose its

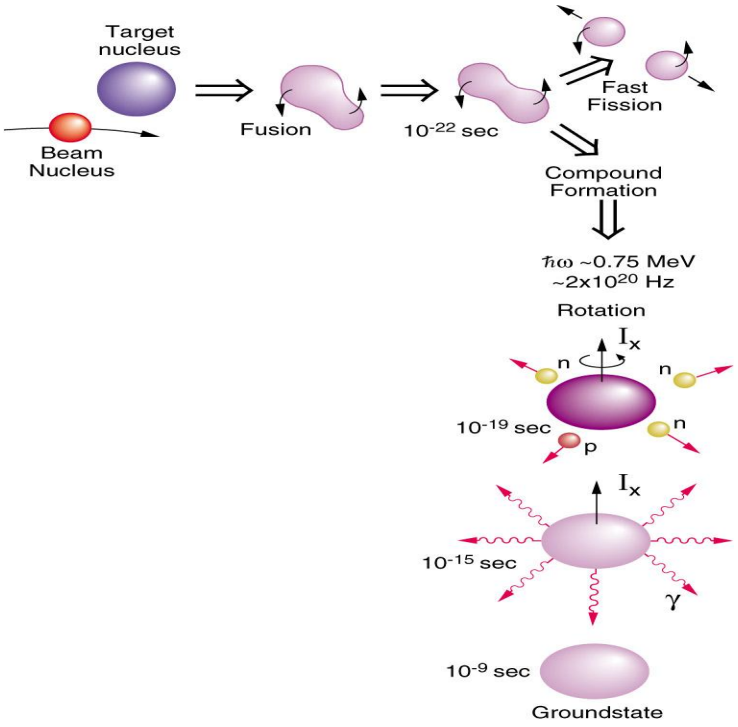

Figure 2.7: Schematic presentation of a fusion-evaporation reaction used to populate high spin states in a nucleus [30].

excitation energy by particle evaporation of α particles, protons or neutrons. However, the Coulomb barrier suppresses charged particle evaporation and thus mostly neutrons are evaporated [31].

The evaporation of particles carries away large amounts of excitation energy, but a small amount of angular momentum. When the excitation energy is below the particle evaporation threshold, the nucleus continues to de-excite through γ-ray emission. The nucleus is still relatively excited and decays by emission of statistical γ-rays. These statistical γ-rays are usually high-energy transitions carrying away large amounts of excitation energy, but again very little angular momentum. These γ-rays are normally not detected in a γ-ray spectrometry experiment. As the cooled nucleus approaches the yrast region, γ-ray emission proceeds through transitions of lower energy carrying more angular momentum to the ground state (see Figure 2.8). It is these yrast-like transitions that are of particular interest to γ-ray spectroscopists, since they carry enough intensity to be isolated

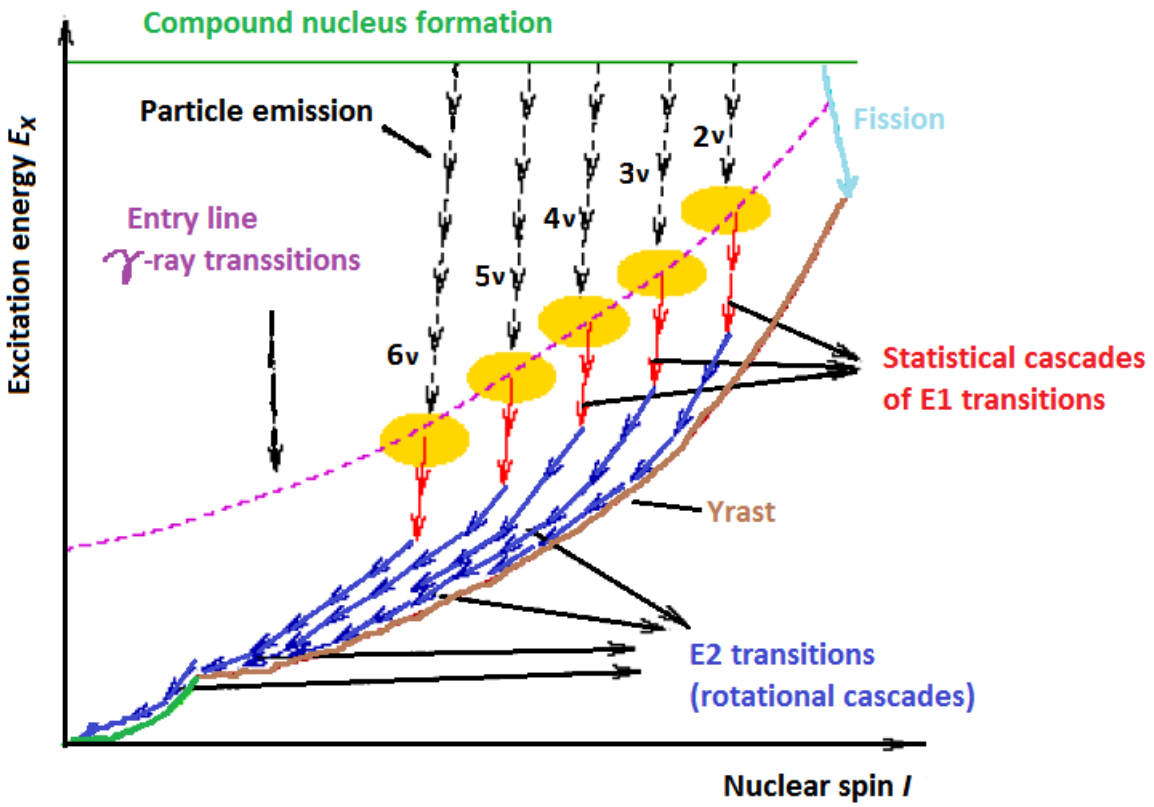

Figure 2.8: This figure shows the steps of the γ-ray decay after a fusion evaporation reaction [32].

in a γ-ray spectrum and can reveal the properties of the nucleus being studied.

Chapter 3

EXPERIMENTAL TECHNIQUES

3.1 Interaction of γ-radiation with matter

Gamma rays are detected through their interactions with the detector material. The relevant interaction mechanisms of γ-rays with matter are photoelectric absorption, Compton scattering and pair production. The relative probability for one of these interactions to occur is a function of the incident photon energy and the atomic number Z of the detector material [17]. These processes are the basis of the detection of γ-rays and are fundamental in measuring different properties of these γ-rays.

3.1.1 Photoelectric effect

The photoelectric effect is the dominant interaction process between photons and matter for γ-ray energies below 200 keV [17] . In this process, the total energy of an incident photon is transferred to a bound atomic electron (most likely a K-shell electron), causing it to be ejected from its atomic orbit with a kinetic energy E_e equal to the initial photon energy E_γ minus the shell binding energy E_b :

$$E_e = E_\gamma - E_b \,. \tag{3.1}$$

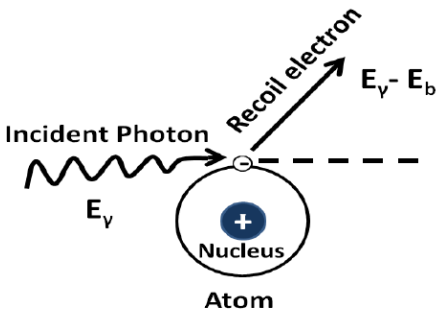

Figure 3.1: The illustration of the process of photoelectric effect [34].

The photoelectric interaction is possible only when the photon has sufficient energy to overcome the binding energy and to remove the electron from the atom. With the loss of an internal electron, the atom is left in an excited state from which it de-excites by emitting characteristic X-ray photons as illustrated in Figure 3.1. If no photon or electron escapes from the detector then all the energy of the incident photon is deposited in the detector. The photoelectric effect is the dominant process when the photon energy is less than 200 keV for germanium. The interaction cross section is given by:

$$\sigma = k\frac{Z^{4.5}}{E_\gamma^3}. \tag{3.2}$$

where k is a proportionality constant and σ is the probability of interaction between a photon of energy E_γ (MeV) and an electron in the material with atomic number Z [33].

3.1.2 Compton scattering

Compton scattering is the process by which a photon scatters from a free or weakly bound electron, resulting in a less energetic photon and a scattered electron carrying the energy lost by the photon (see Figure 3.2). Since the electron binding energy is very small compared to the energy of a γ-ray, the kinetic energy of the ejected electron is nearly equal

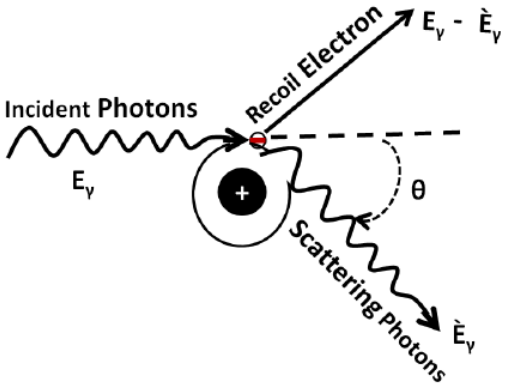

Figure 3.2: Illustration of the Compton scattering process [34].

to the energy lost by the γ-ray and is given by:

$$E_e = E_\gamma - E'_\gamma, \tag{3.3}$$

where E_e is the energy of the scattered electron, E_γ is the energy of the incident γ-ray, and E'_γ is the energy of the scattered γ-ray.

The energy and direction of the scattered γ-ray depend on the amount of energy transferred to the electron during the interaction. The conservation of linear momentum and total energy gives:

$$E'_\gamma = \frac{E_\gamma}{1 + (E_\gamma / m_0 c^2)(1 - cos\theta)}, \tag{3.4}$$

where $m_0 c^2$ is the rest mass energy of the electron = 511 keV, θ is angle between the incident and the scattered photons [17].

When Compton scattering occurs in a detector, the scattered electron is usually stopped in the detection medium and the detector produces an output pulse that is proportional to the energy lost by the incident γ-ray. The energy of the scattered photon varies from a maximum E_γ for $\theta = 0^\circ$ to a minimum for $\theta = 180^\circ$ (head on collision). The Compton

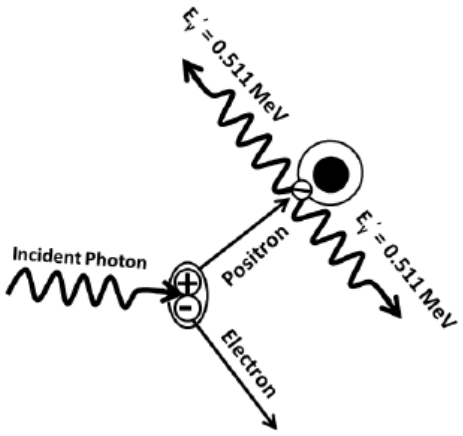

Figure 3.3: The process of pair production [34].

scattering is the dominant interaction for values of energy in the range of 200 - 1000 keV.

3.1.3 Pair production

In pair production, a photon with energy greater than or equal to 1.022 MeV can create an electron-positron pair when it is under the influence of the strong electromagnetic field in the vicinity of a nucleus [35], as illustrated in Figure 3.3. The minimum energy required to create the electron-positron pair is 1.022 MeV. If the γ-ray energy exceeds 1.022 MeV, the excess energy is shared between the electron and positron as kinetic energy. The electron and positron from pair production are rapidly slowed down in the absorber. After losing the kinetic energy, the positron combines with an electron to form photons in an annihilation process. As result two two γ-rays with energies of 0.511 MeV are released. These new γ-rays may interact further with the absorbing material or may escape. The probability of pair production varies approximately as the square of the atomic number Z and is significant in high-Z elements such as lead or uranium [34].

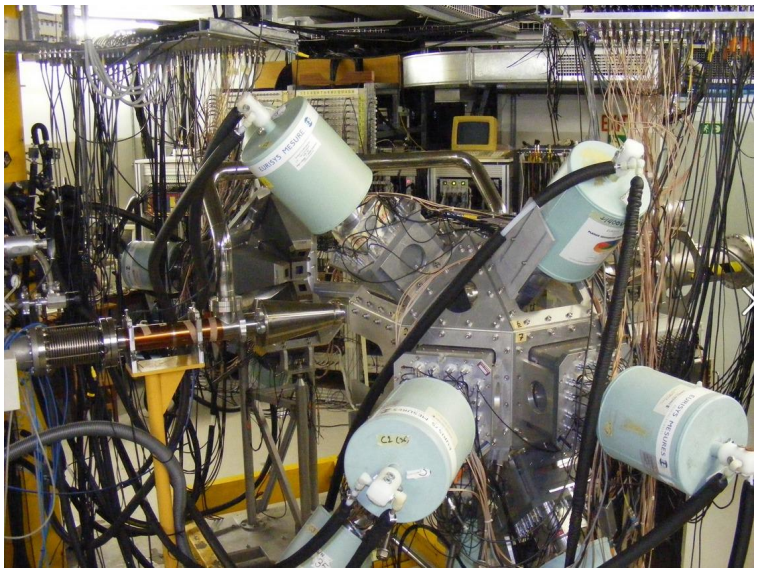

Figure 3.4: The AFRODITE array and the arrangement of the LEPS and clover detectors.

3.2 AFRODITE γ-spectrometer

The γ-rays depopulating high spin states in ^{196}Tl were detected using the AFRODITE γ-spectrometer at iThemba LABS in the Western Cape, South Africa. At the time of the experiment, the γ-spectrometer consists of 8 clover detectors and 6 low energy photon spectrometers (LEPS) detectors (see Figure 3.4). Each clover detector is surrounded by a bismuth germanate (BGO) anti-Compton shield. The shields are used to veto signals from γ-rays that scatter out of the HPGe crystals and therefore they reduce the Compton continuum of the spectra. The detectors are mounted around the target chamber at 45°, 90° and 135° with respect to the beam direction [36]. In this configuration the array has a total photopeak efficiency of $\sim$ 1.6% at 1.3 MeV [21].

The detectors are placed in an aluminium frame structure with 18 squares and 8 triangular facets as shown in Figure 3.5. The target is mounted at the centre of the array, and the beam line passes through the 0° and 180° square facets of the structure.

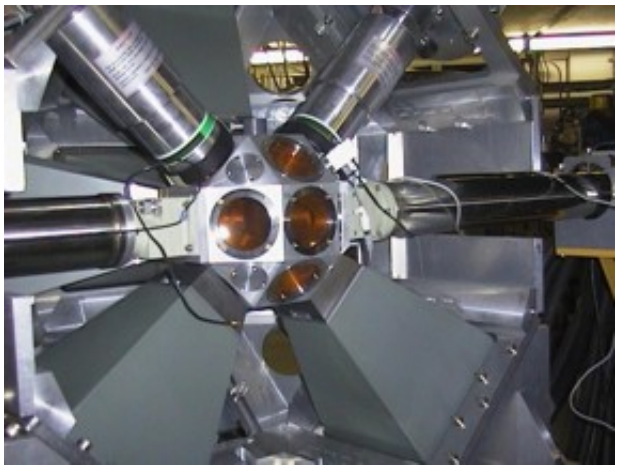

Figure 3.5: The AFRODITE array with the eighteen square facets of the target chamber.

3.2.1 Germanium detectors

Germanium detectors are semiconductor diodes having a p-n structure in which the intrinsic region is sensitive to ionising radiation, such as γ-rays [37]. The device is mounted under reverse bias to increase the depletion region of the diodes. When a photon interacts with the material within the depleted volume of a detector, electron hole pairs are produced. These charge carriers are then converted to a voltage pulse. The number of carriers is proportional to the γ-ray energy and the height of the voltage pulse. Therefore the pulse height is proportional to the γ-ray energy. The voltage pulses are recorded and saved.

Since germanium has a relatively small band gap, the detector must be cooled in order to reduce the thermal generation of charge carriers to an acceptable level. Otherwise, leakage current may induce noise and destroy the energy resolution of the detector. Liquid nitrogen (LN_2) with the temperature of 77 K is the common cooling medium for such detectors. The detector is mounted in a vacuum chamber which is attached to or inserted into a LN_2 cryostat to protect the sensitive detector surfaces from moisture and condensible contaminants.

3.2.2 Clover detectors

The clover detectors consist of four n-type HPGe crystals packed together in a common cryostat [38]. A schematic view of a clover detector is shown in Figure 3.6. Each element of a clover detector has its own pre-amplifier which allows energies deposited in more than one element due to Compton scattering to be added. The primary advantage of using clover detectors over single crystal detectors, is the increased photo-peak sensitivity in add-back mode for γ-rays of energy above 300 keV. In addition, the clover detectors are used as a four-fold Compton polarimeter to allow the measurements of the linear polarisation of γ-rays.

3.2.3 Low energy photon spectrometer (LEPS) detectors

LEPS are planar detectors made of a single crystal of p-type HPGe, electrically segmented into four quadrants, with the dimensions of 10 mm thick and 60 mm in diameter [38]. The signal from each quadrant is processed separately, as in the case of the clovers. The LEPS detectors are efficient in detecting low-energy photons between 5 and 300 keV.

3.2.4 Compton suppression

Because of the Compton scattering interaction, many γ-rays which enter the Ge detector will not deposit their full energy, leading to a large Compton continuum. In order to reduce the contribution of scattered γ-rays, the Ge detector can be surrounded by an escape suppression shield of bismuth germinate Bi_4GeO_{12} (BGO). The BGO shield is used to reject γ-rays which deposit only part of their energy in the Ge before scattering out of the detector. The BGO signal from such an event vetoes the associated clover signal. Figure 3.7 shows the relative positions of the clover Ge detector and BGO suppression shield.

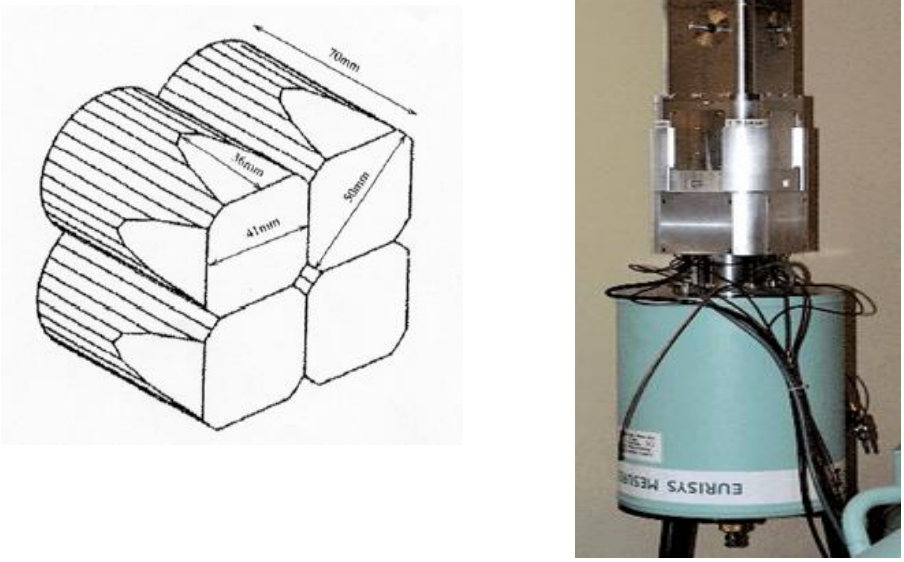

Figure 3.6: The schematic view of the four HPGe crystals in a Clover detector (left), and a clover detector with a tapered rectangular cryostat and cylindrical liquid nitrogen dewar (right) [38].

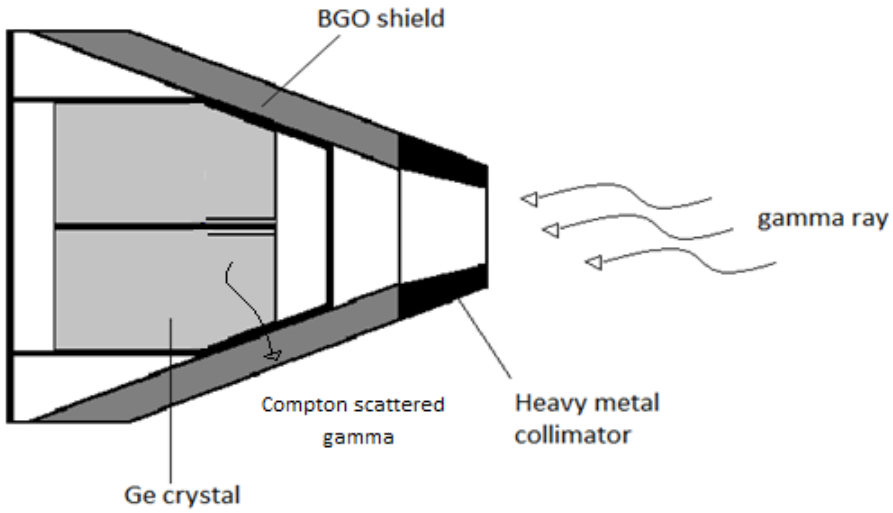

Figure 3.7: A diagram showing the relative positions of BGO anti-Compton shield and the heavy metal collimator of a clover detector [39]

3.2.5 The data acquisition system

In the AFRODITE set up, different steps of data acquisition are used to process signals from the detectors. The Standard Nuclear Instrumentation Module (NIM) and the Computer Automated Measurement and Control (CAMAC) which are located in the AFRODITE vault are used to process signals from the Clover and LEPS detectors. The signals from the Clover detectors are processed by the RIS modules [40] which have integrated circuits such as the standard fast-slow processing and the anti-Compton module. The anti-Compton module vetoes of events with a BGO signal in order to produce clean signals from the Ge detectors. The signals are then feed to the trigger module which requires at least three detectors to fire in coincidence, of which at least two detectors have to be clovers. Once the trigger signal is generated it informs the Analogue to Digital Converter (ADC) and the Time to Digital Converter (TDC) of the RIS module to convert the time and energy signals to digital signals. The ADCs and TDCs of the RIS module are read out by a VME module known as F2VB, then the data is written and stored on tapes for later offline/online analysis. The Multi Instance Data Acquisition System (MIDAS) [41] was used for data sorting.

Chapter 4

EXPERIMENTAL DETAILS

4.1 The experiment

High spin states in ^{196}Tl were populated through the ^{197}Au(^{4}He, 5n)^{196}Tl reaction at a beam energy of 63 MeV. The ^{4}He beam was supplied by the K = 200 separated sector cyclotron facility of iThemba LABS with 40 ns between beam bursts and a pulse selection of 1/7. A thick target of ^{197}Au (3.8 mg/cm^2) was used and the recoils were stopped inside the target. γ-rays emitted from the high-spin states of the residual nuclei were detected by the AFRODITE array. In this experiment, the AFRODITE array was composed of 8 clover detectors and 6 LEPS (at the time of experiment, 2005). 4 clovers and 3 LEPS detectors were placed at 90°, and the others ones were placed at 135° and 45° relative to the beam direction. The LEPS had no time spectra and therefore were not used at all. When the excitation function for the ^{197}Au(α, 5n) reaction is calculated using the code PACE4 [42], it shows that the 5n exit channel peaks at about 61 MeV as shown in Fig. 4.1. The choice of 63 MeV was based on the energy loss consideration of the beam in the target. PACE is a Monte Carlo code that theoretically predicts the cross sections for all possible residual nuclei of a given reaction. The trigger logic required that at least three detectors fired, of which at least two had to be clovers. The coincidence time window

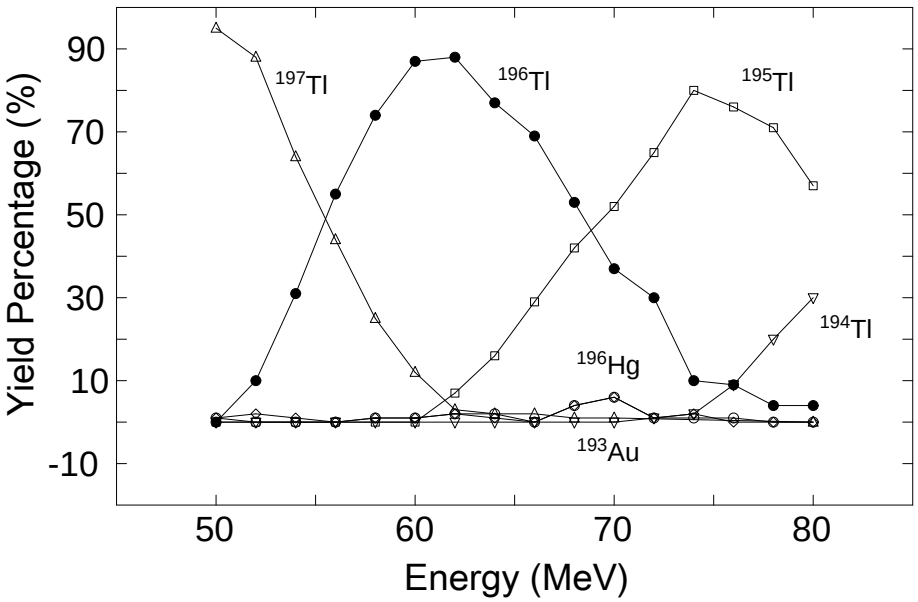

Figure 4.1: Residual nuclei of the ^{197}Au(^{4}He, 5n)^{196}Tl reaction and their percentage yield as function of beam energy calculated with PACE4.

was set to 170 ns.

The data acquisition in this experiment was based on the MIDAS software package described in Ref. [43] and during about 50 hours of beam time, the on-line spectra and event rates were saved on a hard disc in intervals of two hours. The raw event data were written on the digital linear tapes (DLT) for further offline analysis.

4.2 Energy calibration and gain matching

The clover detectors were energy calibrated before performing the experiment by using γ-rays of known energy from standard calibration sources, ^{152}Eu and ^{133}Ba. The spectra from these sources were recorded and the centroids of known peaks were determined using Radware software [44]. In order to sum the data from different detectors, the detectors

were gain-matched through the quadratic relation:

$$x' = 2E = ax^2 + bx + c \tag{4.1}$$

where x' is the channel number of the peak in the gain-matched spectrum, x is the channel number of the peak in the original (non-gain-matched) spectrum of the ^{152}Eu peak with energy E. The gain matching coefficients a, b, c are determined for each detector. The quadratic equation is transformed in a linear equation as E (keV) $= 0.5\, x'$ so that the matched gain of spectra has a gain of 0.5 keV/channel.

4.3 Gain drift corrections

Temperature fluctuations in the electronics during the experiment often alter the gain of the detector. This leads to the variation of the peak position with respect to its initial position, during the course of the experiment. To make a gain drift correction, a reference spectrum is needed which is usually the gain matched and calibrated spectrum from the first run. The gain drift was found to be a linear function of the channel number.

$$x' = 2E = a_1 x + a_0 \tag{4.2}$$

where x' is the channel number of the peak in the gain matched spectrum, x is the channel number of the peak in the original (non-gain matched) spectrum of the ^{152}Eu peak with energy E. The gain drift correction coefficients a_1 and a_0 are determined for each run. There were 31 runs of data in this experiment. Two reference peaks are to be chosen, one at higher energy (P_h) and the other at low energy (P_l). If we consider $P + S$ as the position of the shifted peak and P as the reference peak, a_1 and a_0 the originally gain coefficients and a_1' and a_0' the new coefficients, the positions of shifted and reference peaks at lower and higher energy are: $P_l + S_l = a_1\, x + a_0$, $P_l = a_1'\, x + a_0'$, $P_h + \mathrm{S}_h = a_1\, y + a_0$

and $P_h = a'_1\ y\ +\ a'_0$. Solving the equations we obtain:

$$a'_1 = a_1 \frac{P_h - P_l}{(P_h - P_l) + (S_h - S_l)}\ , \tag{4.3}$$

$$a'_0 = a_0 \frac{P_h - P_l}{(P_h - P_l) + (S_h - S_l)} + \frac{P_l S_h - P_h S_l}{(P_h - P_l) + (S_h - S_l)}\ . \tag{4.4}$$

The new coefficients a'_1 and a'_0 are gain and offset respectively and are used when sorting the data. With the new coefficients, the previously gain-drifted peaks are observed at the same channel numbers with the reference spectrum.

4.4 Detector efficiency and efficiency calibration

The efficiency measurements of the clover and LEPS detectors were performed using the standard calibration sources of ^{152}Eu and ^{133}Ba. The percentage efficiency of the present experiment is shown in Fig. 4.2 which shows that the AFRODITE array had maximum relative efficiency in the energy range 130-140 keV.

4.5 Construction of γ-γ matrices

After the gain matching coefficients from the gain-drift and Doppler shift corrections were available, they were used to sort data into an $E_{\gamma 1}$-$E_{\gamma 2}$ matrices. Two γ-rays $E_{\gamma 1}$ and $E_{\gamma 2}$ are said to be in coincidence if they are detected within the coincidence time window. The γ-rays detected in coincidence constitute a coincidence event. In this experiment the $E_{\gamma 1}$-$E_{\gamma 2}$ coincident matrix consisted of a two dimensional matrix of γ-γ events with $E_{\gamma 1}$ on the x and y-axes and coincidence counts on the z-axis. Let us consider a coincident event of three γ-rays, e.g. $E_{\gamma 1}$, $E_{\gamma 2}$ and $E_{\gamma 3}$. The possible coincidence pairs one can form are: ($E_{\gamma 1}$, $E_{\gamma 2}$), ($E_{\gamma 2}$, $E_{\gamma 1}$), ($E_{\gamma 1}$, $E_{\gamma 3}$), ($E_{\gamma 3}$, $E_{\gamma 1}$), ($E_{\gamma 2}$, $E_{\gamma 3}$) and ($E_{\gamma 3}$, $E_{\gamma 2}$). The coincidence pairs are represented in a matrix, by coordinates (x, y, z) and the pair

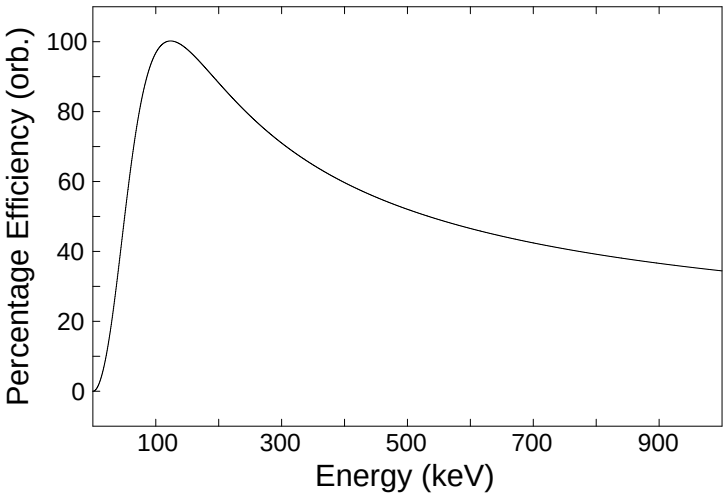

Figure 4.2: The normalised efficiency of the clover detectors as function of γ-ray energy.

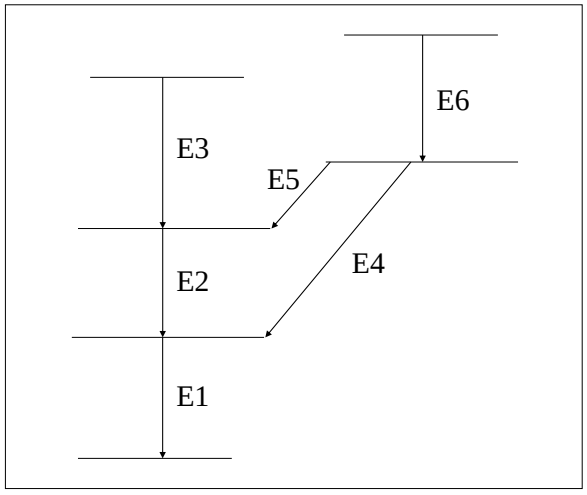

Figure 4.3: A simple level scheme of 5 transitions.

($E_{\gamma 1}$, $E_{\gamma 2}$) correspond to coordinates ($E_{\gamma 1}$, $E_{\gamma 2}$, $z_{\gamma 12}$) while the pair ($E_{\gamma 2}$, $\mathrm{E}_{\gamma 1}$) correspond to coordinates ($E_{\gamma 2}$, $E_{\gamma 1}$, z_{21}). The coordinate z_{12} represents the number of instances the pair ($E_{\gamma 1}$, $E_{\gamma 2}$) is found in the data. Similarly z_{21} represents the number of instances the pair ($E_{\gamma 2}$, $E_{\gamma 1}$) is detected in the data. If the matrix is symmetric, $z_{12} = z_{21}$. For every instance a coincidence pair ($E_{\gamma 1}$, $E_{\gamma 2}$) is detected, the coincidence count coordinate z, is incremented. In general the matrix is constructed by incrementing the corresponding coincidence counts *e.g* z_{12}, for a specific pair each time this pair is found in the data.

In this experiment data were sorted into four matrices. The first one was a symmetric γ-γ coincidence matrix which was used to construct the level scheme. The second was an asymmetric directional correlation (DCO) matrix, used in assigning spin and parity to nuclear states. The third and fourth were a pair of polarization matrices, used in polarization analysis, for the purpose of spin and parity assignments.

4.6 Gating

Gating is a way of identifying whether a γ-ray is in coincidence with other γ-rays. Gating on a particular γ-ray energy, only γ-rays that are in coincidence with the gated one are shown. This refers to the slicing of a region around a γ-ray energy E_γ on the x or y axis in a E_γ-E_γ matrix and projecting all the γ-rays in coincidence with the γ-ray with energy E_γ into a one-dimensional spectrum. By inspecting different gates on different γ-ray energies, the level scheme of a nucleus can be constructed. Let us consider a simple level scheme shown in Fig. 4.3. If a gate is set on the transition $E1$, all the other γ-rays in this level scheme are seen in the spectrum because they are in coincidence (they belong to the same decay path as the $E1$ transition). However if the gate is set on the transition $E2$, then $E3$, $E5$ and $E6$ will be seen but $E4$ will not be seen in the spectrum because it is not in coincidence with $E2$ (they do not belong to the same decay path). With such gating analysis, one can locate and place the γ-rays and build a level scheme.

4.7 Construction of the level scheme

The construction of the level scheme is done from the analysis of the coincidence relationships between the detected γ-rays by means of gating with the use of the ESCL8R software program [45]. Usually one starts with a few already-known transitions, and by gating on these, γ-rays in coincidence are observed in the spectrum and are placed according to the coincidence relation between them. Thus a level scheme can be built. In this work the previously known level scheme of ^{196}Tl was taken from [7] and is shown in 5.1. With γ-γ coincidence analysis several new transitions were placed in the ^{196}Tl level scheme which are discussed in the chapter 5.

4.8 DCO ratios

The Directional Correlation from Orientated states (DCO) method can be used to determine the multipolarity of γ-ray decays and to infer the spin of states in a level scheme. The DCO ratio measurement is similar to angular distribution measurements and is often used with small arrays or when γ-rays with small intensities are measured [21]. To determine the multipolarities of the γ-ray transitions in ^{196}Tl, the coincident events were sorted into an asymmetric matrices with data from the 90° detectors on one axis and 135° detectors on the other axis. In this work, the R_{DCO} were measured by gating on known multipolarity ($E2$) transitions and measuring the ratios of coincidence intensity(I) at two angles 90° and 135° according to the expression

$$R_{DCO} = \frac{W(135°, 90°)}{W(90°, 135°)} \,, \tag{4.5}$$

where $W(135°, 90°)$ is an angular correlation function and denotes the intensity of a γ-ray detected at 135° when a gate is set on an $E2$ γ-ray detected by a detector at 90° with respect to the beam direction. In the present work, when a gate was set on a known

stretched $E2$ transition, the $R_{DCO} \approx 1.0$ and 0.6 values were observed for the known $E2$ and $E1$ transitions respectively, and when a gate was set on a known stretched $E1$ transition, the $R_{DCO} \approx 1.6$ and 1.0 values were found for known $E2$ and $E1$ transitions respectively. The R_{DCO} values for newly observed transitions were measured and compared with the theoretical predictions calculated using the code DCOplot as described in [46] for the purpose of determining the multipolarity of the transitions.

4.9 Linear polarization measurement of γ-rays

The R_{DCO} values make no distinction between electric and magnetic transitions. Thus, it was necessary to perform the linear polarization measurements to deduce the electric or magnetic character of the transition to allow us to assign spin and parity to levels. In this way, clover detectors situated perpendicular to the beam direction were used as Compton polarimeters to scatter the incident γ-rays. Two E_γ-E_γ matrices were constructed where one contained γ-rays scattered perpendicular to the beam direction in coincidence with any detected γ-ray and the other contained γ-rays scattered parallel to the beam direction in coincidence with any detected γ-ray. The linear polarization anisotropy P, defined as

$$P = \frac{A}{Q}\,, \tag{4.6}$$

is determined on the basis of the experimental asymmetry between vertically and horizontally-scattered γ-rays:

$$A_P = \frac{aN_V - N_H}{aN_V + N_H}\,, \tag{4.7}$$

where N_V and N_H are the number of γ-rays scattered in vertical and horizontal directions respectively and a is the polarisation sensitivity of the detector crystals, typically very close to 1, determined using unpolarized γ-rays from a ^{152}Eu source. The Polarization

sensitivity Q for clover detectors has been measured [47] to be

$$Q = Q_0[0.31 + 7x10^{-5}E_\gamma] \,, \tag{4.8}$$

where E_γ is in keV. Q_0 is the polarization sensitivity for an ideal polarimeter:

$$Q_0 = \frac{1+\alpha}{1+\alpha+\alpha^2} \,, \tag{4.9}$$

where $\alpha = E_\gamma[\text{keV}]/511$.

The linear polarization measurements do not depend on the multipolarity of gating transition thus it did not matter if a gate was set on a quadrupole or a dipole transition. The A_P measured values were compared to the calculated A_P values using the code POLAR [48] when assigning spin-parity to levels. The code POLAR is a program designed to predict the A_P value of a transition depending on its multipolarity and its character. In this way the transitions with positive A_P values were interpreted as stretched electric or unstretched magnetic and those with negative A_P values were interpreted as stretched magnetic or unstretched electric transitions.

Chapter 5

RESULTS

This chapter confirms the placement of previous γ-rays in ^{196}Tl nucleus and confirms also those which were tentative. It discusses the newly observed γ-rays and places them in the level scheme. It discusses also the assignment of spin and parity to new levels, using the *DCO* ratio and polarization measurements of transitions.

5.1 Level scheme and new levels

The first step of data analysis was to confirm the existing level scheme and extend it if possible. The known level scheme of ^{196}Tl was taken from ref. [7] and consists of 29 levels and 38 transitions grouped in 3 bands as shown in Figure 5.1. The isomeric level 7^+ ($T_{1/2}$ = 1.41 h) at energy of 395 keV decays with a branching of 96.2% to ^{196}Hg [49] via electron capture and represents for us an effective ground state from which we have built the new level scheme. The highest observed level was a tentative $I^\pi = (20+I_0^-)$ at excitation energy of (3630.5 + x) keV or (3236 + x) keV with respect to 7^+ isomer. The additional level I_0 at excitation energy 738.6 + x was suggested by Kreiner *et al.* [7] to account for the unobserved γ-ray ($\sim$ 35 keV) above the 8^- isomer level (see Figure 5.1). This highly electron-converted γ-ray transition is predicted by the theory of odd-even staggering in the excitation energies of Band 1 in odd-odd Tl nuclei [11]. In the present

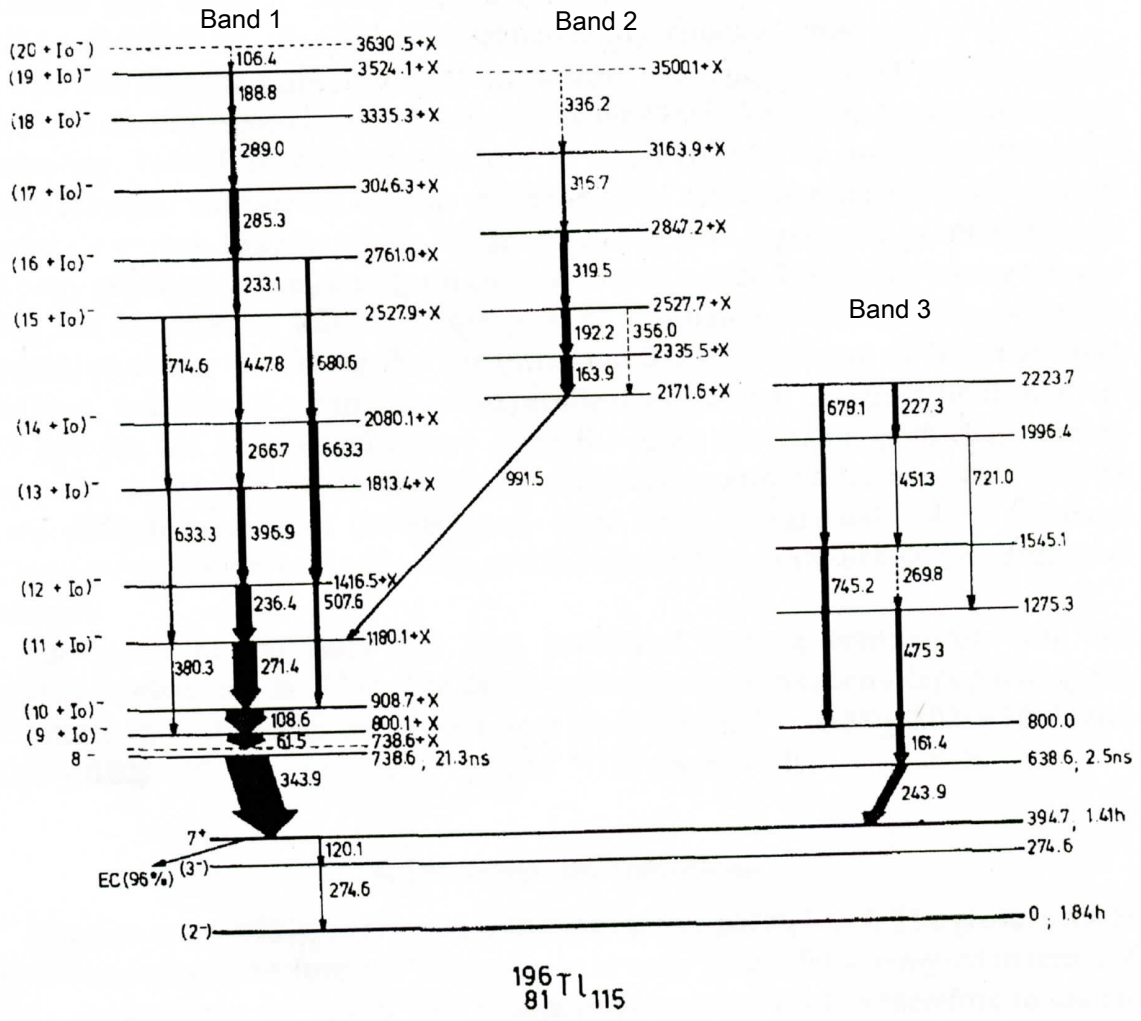

Figure 5.1: The known level scheme as established by Kreiner *et al.* [7]

work, the previous level scheme was checked using coincidence and intensity relations. The known level scheme was extended up to $I^{\pi} = (21^{-})$ at excitation energy $E_x = (4071)$ keV with respect to 7^{+}, and several side feeding transitions were observed. A total of 13 new levels and 24 new γ-rays were found and placed in the new proposed level scheme as shown in Figure 5.2. The spins and excitation energies of levels above the 8^{-} level are tentative because of the unknown offset I_0, and therefore they appear in parentheses. In the following we will discuss only the confirmation of the previously tentative γ-rays in ^{196}Tl and the observation and placement of new γ-rays following their respective bands.

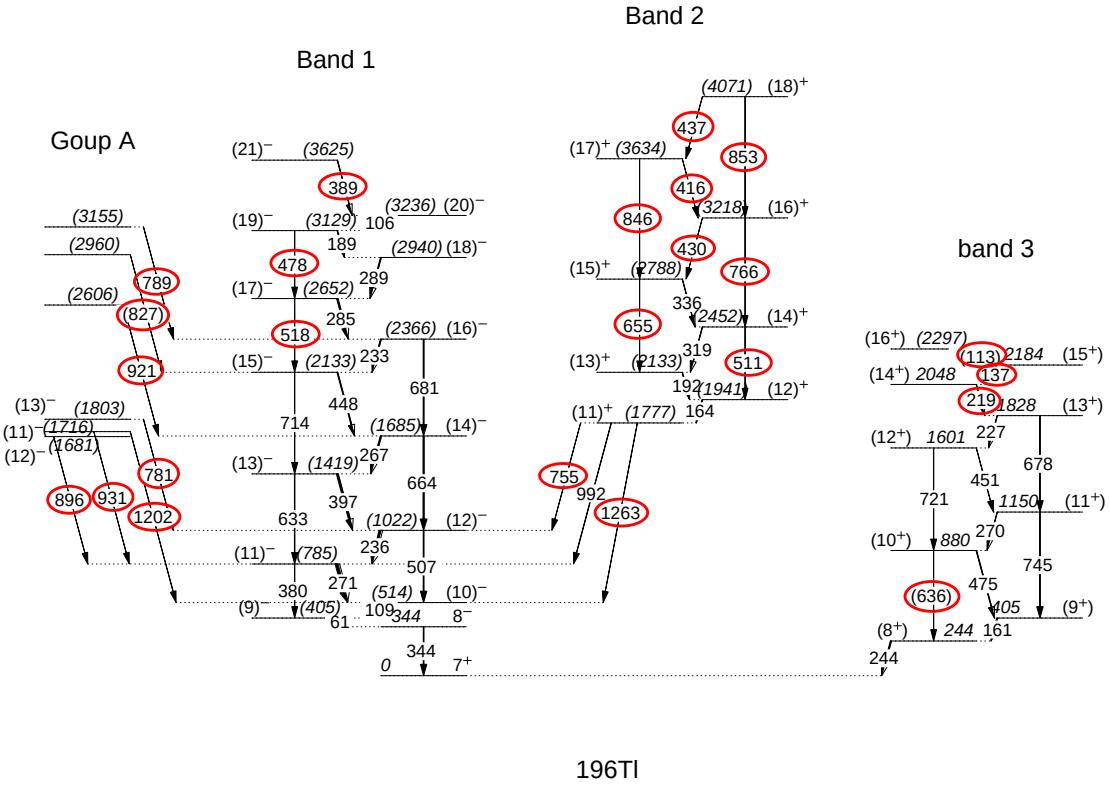

Figure 5.2: The level scheme proposed in the present work. The spins and excitation energies in Band 1 are tentative because of the shift of the level predicted by Kreiner *et al.* [7] above the 8^- level. Newly-added γ-rays are encircled.

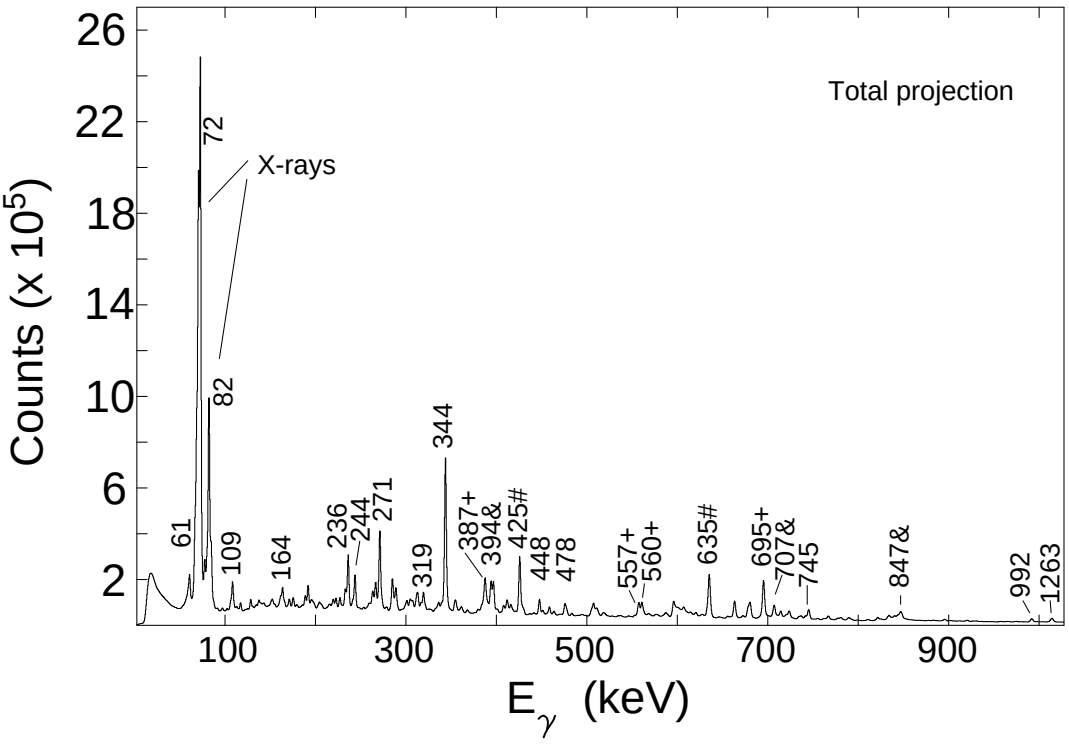

Figure 5.3: In the total projection spectrum peaks of most Band 1 transitions in ^{196}Tl are clearly seen. The labelled peaks are from ^{195}Tl (&), ^{196}Hg (#) and ^{197}Tl (+) contaminants.

5.1.1 Band 1

Band 1 of ^{196}Tl was previously established up to a tentative spin of $(20)^-$ at excitation energy of (3236) keV in the present scale. It represents a cascade of $\Delta I = 1$ in-band transitions along with $\Delta I = 2$ cross-over transitions based on the isomer level 8^- ($T^{1/2} = 21.3$ ns) which decays to the 7^+ isomer level ($T^{1/2} = 1.4$h) via an E2, 344 keV transition as shown in Figure 5.2.

Band 1 is stronger in the data compared to the other bands. The total projection spectrum shown in Figure 5.3 shows strong peaks of transitions in Band 1 and other peaks from ^{195}Tl, ^{195}Hg and ^{197}Tl residual nuclei labelled with symbols &, # and + respectively. A gate set on the strongest peak 344 keV (see Figure 5.4), shows most of the peaks of the established γ-rays of Band 1 and newly observed γ-rays marked with symbol $*$.

To confirm the tentative 106 keV γ-ray transition, $(20)^- \rightarrow (19)^-$, a gate was set on

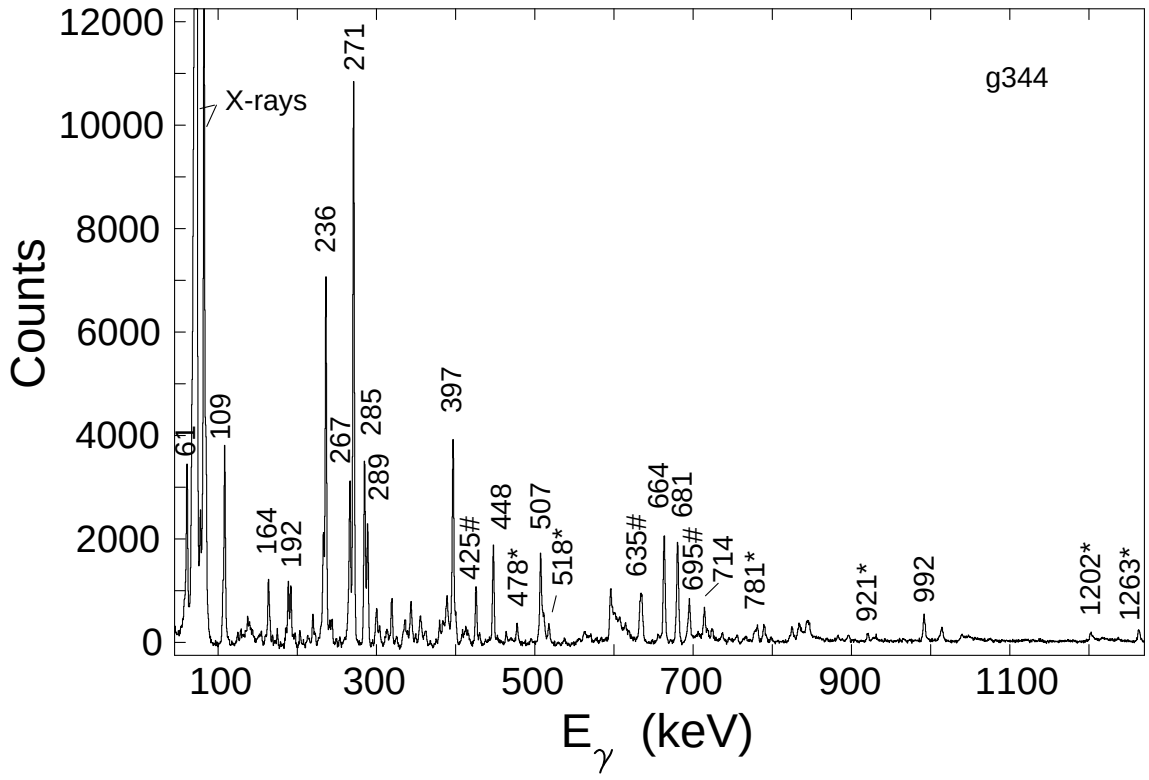

Figure 5.4: Coincidence spectrum gated on the 344 keV transition. Strong peaks of known γ-ray transitions of Band 1 are seen and new transitions (marked as $*$) are also seen. The peaks with # label are contaminants from ^{196}Hg. The triangular peak to the left of the 635 peak is associated with the neutron interacting with the detector.

the 189 keV transition (see Figure 5.5 (a)). The spectrum of this gate shows most of the Band 1 transitions and a peak of 106 keV on the shoulder of the 109 keV ($(10)^- \rightarrow (9)^-$) peak. A spectrum gated back on 106 keV shown in Figure 5.5 (b), shows a clear peak of 109 keV together with most of the γ-rays of Band 1. This indicates that the 106 keV transition is in coincidence with Band 1 transitions and is a member of the band. To confirm its placement, the coincidence intensity ratio was considered. The measured I_{106}/I_{189} from a gate set on the 289 keV transition gave a value of 0.6. A value less than 1 indicates that the 106 keV γ-ray should probably be placed above the 189 keV transition and it was therefore placed there.

After confirmation of the existing γ-ray transitions of Band 1, the next step was to

find new transitions in this band by gating. A gate set on the 189 keV transition shown in Figure 5.5 (a) shows a new transition of 389 keV. A spectrum gated on 389 keV in turn (Figure 5.5 (c)), shows strong peaks of Band 1 transitions and a lot of contaminants from ^{197}Tl. This is because the ^{197}Tl, a residual nucleus of the reaction, has a strong 388 keV γ-ray in its low lying transitions. As most of Band 1 transitions are seen in the spectrum, it is likely that the 389 keV transition belongs to Band 1 of ^{196}Tl and should be placed there. To place this transition on the top of the band, it was necessary to measure the coincidence intensity branching ratio. The measured $I_{189}/I_{478} = 0.31$ gated on 106 keV was compared to the $I_{189}/I_{478} = 0.35$ when a gate was set on 389 keV. The obtained similar intensity branching ratio values suggest that the 389 keV and 106 keV γ-rays are likely in the same decay path with the 189 keV and 478 keV transitions and therefore the 389 keV should be placed above the 106 keV transition. With addition of the new 389 keV transition, Band 1 was extended up to an excitation energy of (3625) keV.

Two new cross-over $\Delta I = 2$ transitions not observed by Kreiner *et al.* were found to decay to higher spin states of Band 1. These are the 518 keV ($(17)^- \rightarrow (15)^-$) transition that decays parallel to the 285 keV and 233 keV transitions and the 478 keV ($(19)^- \rightarrow (17)^-$) transition that decays parallel to 289 keV and 189 keV transitions. These transitions were observed as follows: 518 keV and 478 keV peaks are observed in the spectrum gated on the 106 keV transition (Figure 5.5 (b)). A gate set on the 448 keV, a Band 1 transition (Figure 5.6 (a)), shows clearly the 518 keV and 478 keV transitions. A gate set on 518 keV in turn (Figure 5.6 (b)), shows Band 1 transitions but the parallel decay, 285 keV and 233 keV transitions are not seen as expected. As 285 keV + 233 keV = 518 keV, it indicates that 518 keV is a cross over of 285 keV and 233 keV transitions. A gate set on the 478 keV (Figure 5.6 (c)) shows Band 1 transitions with a lot of contaminants from^{196}Hg. This is because the ^{196}Hg which is a residual nucleus in the reaction, has a very strong 478 keV γ-ray in its low lying transitions. As Band 1 transitions of ^{196}Tl can be seen in the spectrum of 478 keV gate, it is most probably that the 478 keV transition belongs

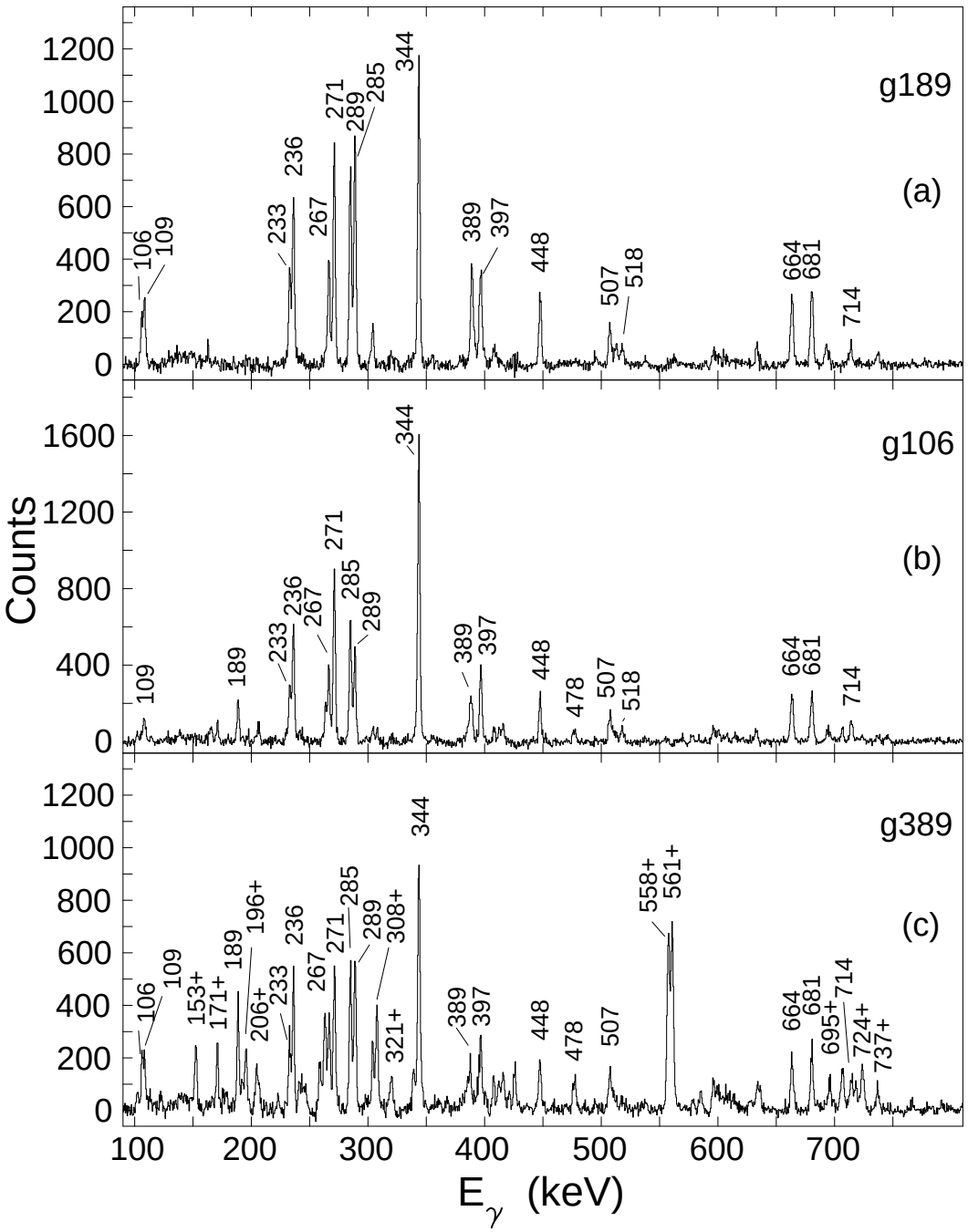

Figure 5.5: The coincidence spectrum gated on the 189 keV (panel (a)) shows the tentative 106 keV and the new 389 keV transitions. Transitions in Band 1 of ^{196}Tl can be seen in the 106 keV gate (panel (b)) and in the 389 keV gate (panel (c)). The peaks labelled with + in (panel (c)) are the contaminants from ^{197}Tl.

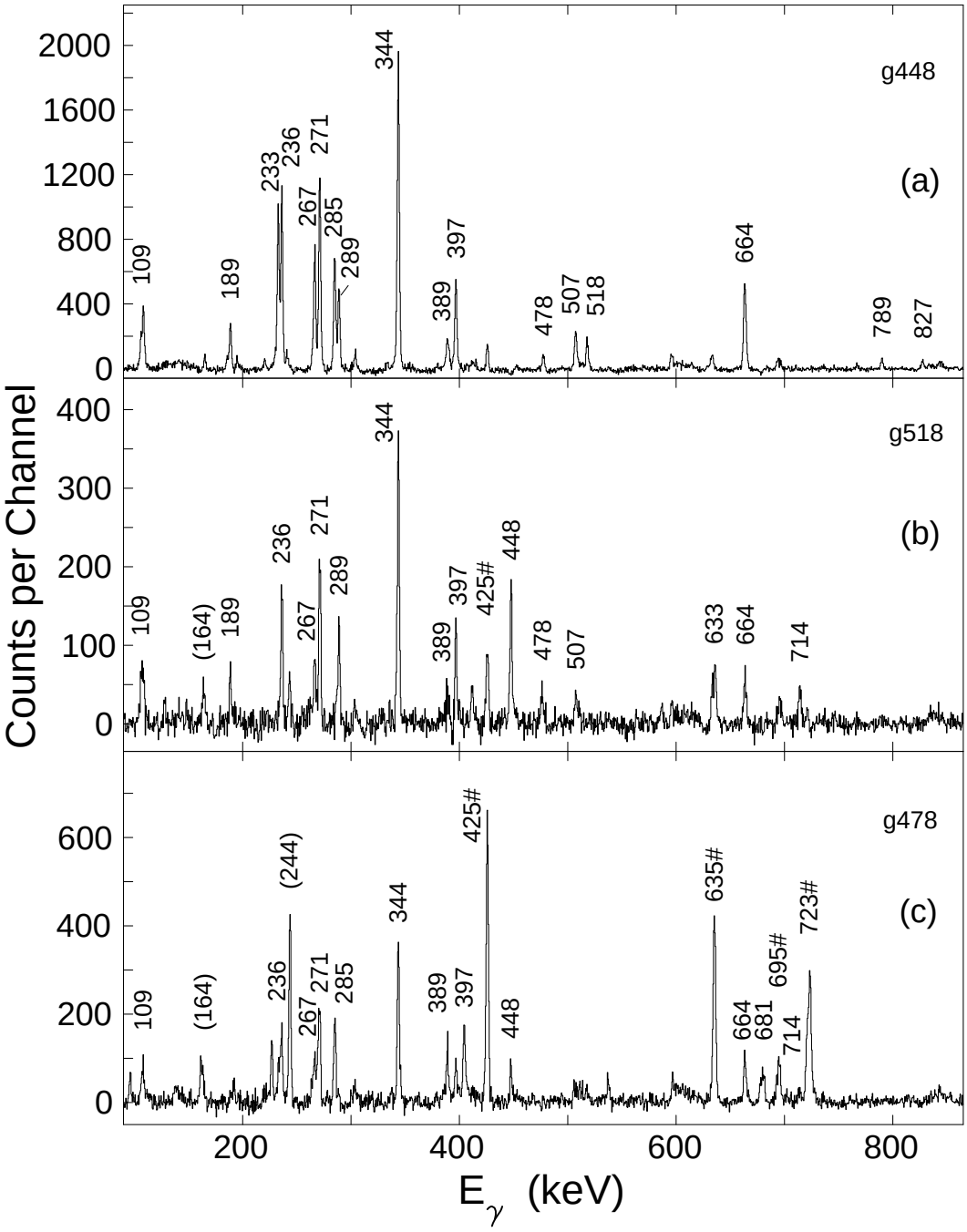

Figure 5.6: Panel (a) shows a gate set on the 448 keV in Band 1. It shows clearly two new transitions of 518 keV and 478 keV. The gates set on the 518 keV and 478 keV, panel (b) and (c) respectively show clearly transitions of Band 1. The peaks with number of energy in parenthesis belong to Band 3. The peaks with # symbol are the contaminants from ^{196}Hg.

also to this band. Further, a closer look in the spectrum indicates that the 289 keV and 189 keV transitions are not seen in the spectrum. Since 478 keV = 189 keV + 289 keV it is likely that the 478 keV cross-over parallel to 189 keV and 289 keV transitions and thus it should be placed there.

5.1.2 Energy levels decaying to Band 1

Several new levels were found to decay into Band 1 from the side. These levels have been labelled "Group A" for convenience and it is not clear if they are associated with the same intrinsic configuration. The transitions 781 keV, 789 keV, 827 keV, 896 keV, 921 keV, 931 keV and 1202 keV connect levels of "Group A" to levels of Band 1. These transitions are observed in the spectrum gated on 344 keV ($8^- \rightarrow 7^+$) of Band 1 shown in Figure 5.7 (a), and are labelled ($*$). These new transitions were gated on back to be sure if they are in coincidence with transitions of Band 1 in ^{196}Tl nucleus.

The spectra gated on the 896 keV and 931 keV shown in Figure 5.8 (a) and (b) respectively, see the known established 61 keV ($(9)^- \rightarrow 8^-$) shown in the corner of the spectra. They also see the 109 keV ($(10)^- \rightarrow (9)^-$), 271 keV ($(11)^- \rightarrow (10)^-$), and 344 keV ($8^- \rightarrow 7^+$) transitions of Band 1 but no established transitions of ^{196}Tl above the 11^- level are observed in the two spectra. Thus, it is most likely that the 896 keV and 931 keV transitions decay to the same level ($I^\pi = (11)^-$) of Band 1 from the side.

The spectrum gated on the 1202 keV, shown in Figure 5.8 (c), shows the established transitions of Band 1 placed below the $(10)^-$ level which are 61 keV, 109 keV and 344 keV. No known transitions of Band 1 above this level are seen. The spectrum shows also the same peaks observed in the 931 keV and 896 keV gates except the 271 keV peak. Further 931 + 271 = 1202 suggests that 1202 keV is a cross-over of 931 keV and 271 keV. Thus the 1202 keV was placed parallel to the 931 keV and 271 keV transitions in the new level scheme.

A gate set on the 781 keV peak observed in the 344 keV gate, shows the established

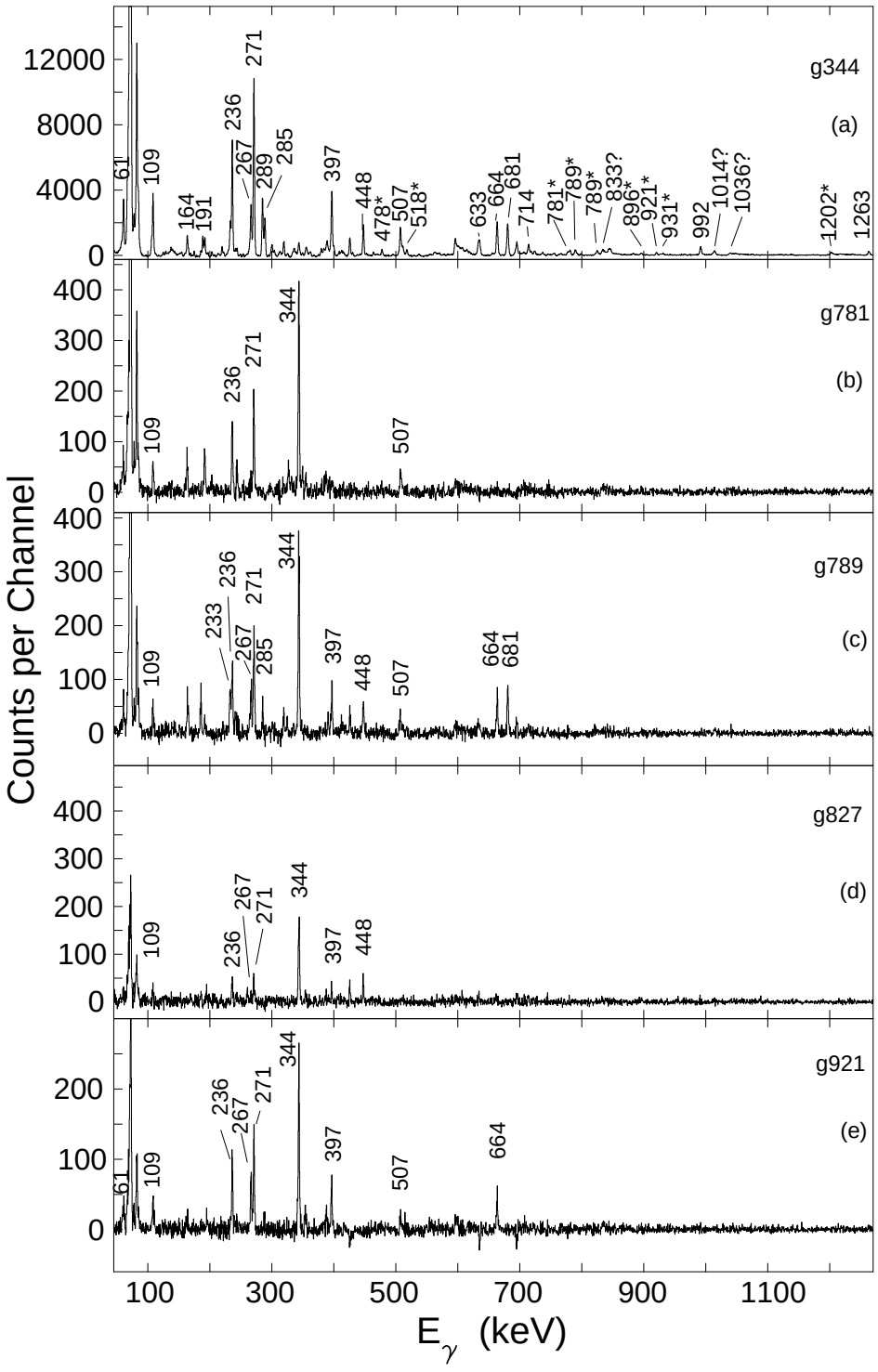

Figure 5.7: This figure shows a number of spectra obtained by setting a gate on number of transitions feeding to Band 1 of ^{196}Tl. For example panel (a) is labelled g344 which means a spectrum gated on 344 keV. The peaks labeled with the symbol $*$ represent new transitions decaying in Band 1 and those labelled with ? denote transitions that could not be added to the level scheme.

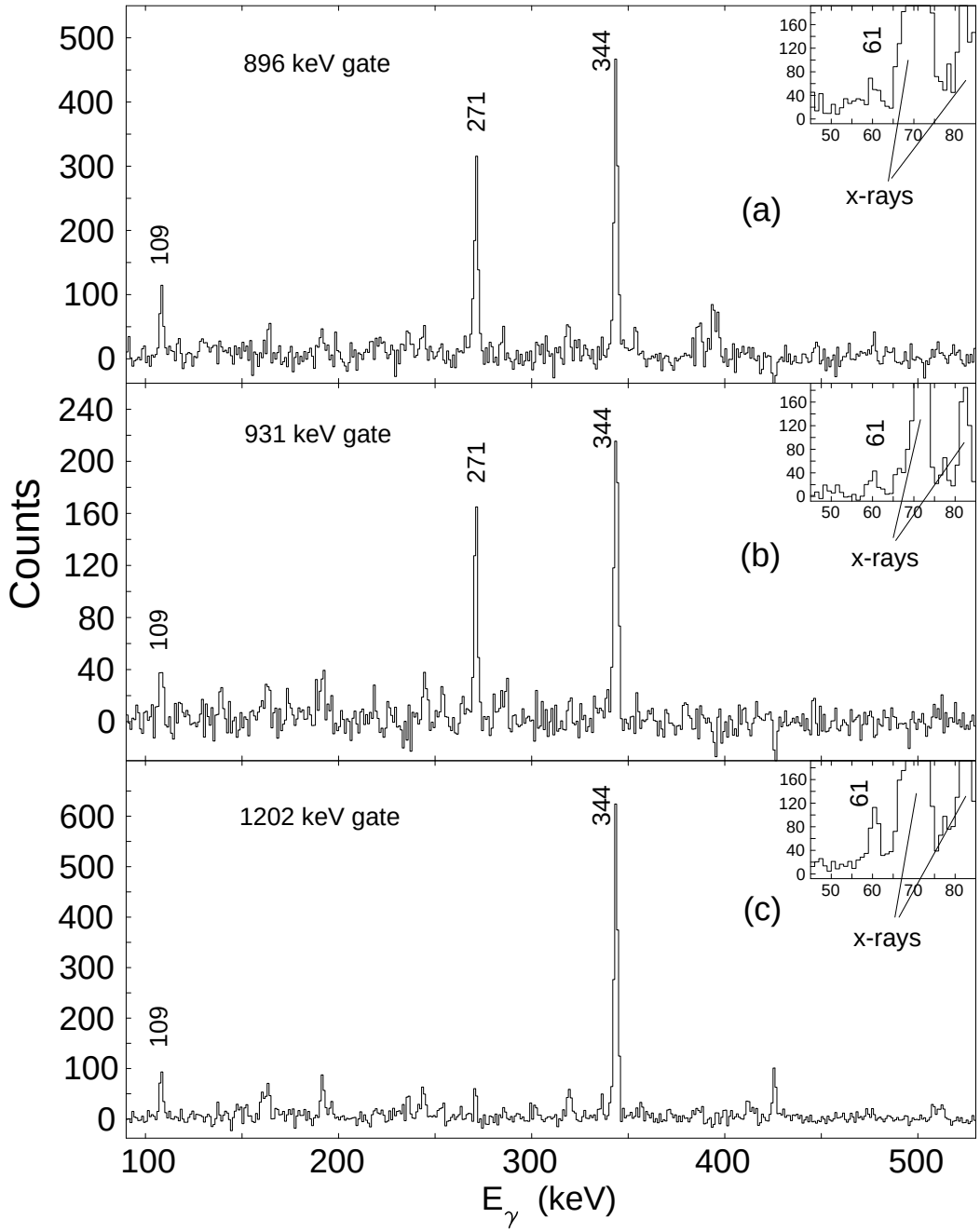

Figure 5.8: Panel (a), (b) and (c) show coincidence spectra obtaining by setting gates on 896 keV, 931 keV and 1202 keV respectively. These transitions all feed into Band 1. The non-labelled peaks are contaminants from other residual nuclei.

transitions 109 keV, 236 keV, 271 keV, 344 keV and 507 keV of Band 1. No established transitions above the $(12)^-$ level are seen in the spectrum (Figure 5.7 (b)). As result, the 789 keV transition was placed to populate the $(12)^-$ level from the side.

The spectrum gated on the 921 keV which is observed in the 344 keV gate, shows the established transitions of 109 keV, 271 keV, 236 keV, 267 keV, 344 keV and 397 keV of Band 1 placed below the $(14)^-$ level. The established cross over 507 keV and 664 keV transitions are also seen. No established transition above the $(14)^-$ level are seen in the spectrum (Figure 5.7 (e)). For this reason the 921 keV transition was placed to populate the $(12)^-$ state from the (2606) keV side level.

The spectrum gated on the 827 keV shown in Figure 5.7 (d) shows the known transitions of Band 1 placed below the $(15)^-$ level of 109 keV, 271 keV, 236 keV, 267 keV, 344 keV, 397 keV and 448 keV, but the expected cross-over E2 transitions of 507 keV, 664 keV, 633 keV and 714 keV are not seen. Probably this transition is very weak and no statistics can be obtained. As result, the 827 keV was placed as a tentative transition that feeds the $(15)^-$ level of Band 1 from the side.

The spectrum gated on the 789 keV peak observed in the 344 keV gate, shows the established transitions of 109 keV, 271 keV, 285 keV, 236 keV, 267 keV, 344 keV, 397 keV, 448 keV and cross-over 507 keV, 664 keV and 681 keV of Band 1 placed below the $(17)^-$ level. But no known transition above this level is seen in the spectrum (Figure 5.7 (c)). Thus the 789 keV was placed to decay to the $(18)^-$ level of Band 1 from the side.

There are other peaks which were seen in the 344 keV gate but could not be placed in Band 1 of the ^{196}Tl nucleus. These are the 833 keV, 1014 keV and 1036 keV peaks labelled as (?) in the upper panel of Figure 5.7 (a). These peaks could also not be found in any other neighbouring nuclei.

5.1.3 Band 2

Band 2 was established previously up to an excitation energy of (3500.1 + x) keV or (3105) keV with respect to the 7^+ isomer. In this work we have extended this band up to an excitation energy of (4071) keV (with respect to 7^+) and a total of 10 transitions have been found and added. The new transitions were observed and placed following the coincidence relations and intensity.

The 316 keV γ-ray previously placed above 319 keV in Band 2 [7] was removed from the band. This γ-ray is not seen in the spectrum gated on the 164 keV transition of Band 2 shown in Figure 5.9 (a) or in any spectrum gated on the transition of this band. A gate set on 316 keV (shown in Figure 5.9 (b)) does not show any transition of Band 2. It rather shows transitions found to belong to ^{195}Tl. As 316 keV seems not to be in coincidence with Band 2, it implies that this γ-ray was wrongly placed in Band 2 and was removed.

A tentative 336 keV transition was confirmed in this work as follows: A gate set on 164 keV (Figure 5.9 (a)) shows a peak of 336 keV clearly seen in this spectrum. A gate set on 336 keV (Figure 5.9 (c)), shows the known transitions and new transitions (labelled with $*$) of Band 2 together with the linking transition 992 keV. Thus, the 336 keV is likely a transition of Band 2 and it was placed above 319 keV following the intensity relation.

The previous tentative 356 keV transition in Band 2 is seen in the spectrum gated on 336 keV (Figure 5.9 (c)). However, the 356 keV peak is also seen in the gate set on 164 keV for which it is in anti-coincidence. Further, a gate set on 356 keV shows most of the peaks (labelled with #) which do not belong to Band 2 (see Figure 5.10 (a)). The anti-coincident 164 keV and 192 keV are also seen in the spectrum. A gate set on the 992 keV link (Figure 5.11 (b)) does not show the 356 keV peak as we would expect. Consequently the tentative 356 keV does not show any evidence to be in Band 2 and was removed.

To find new transitions in Band 2, a gate was set on the 164 keV γ-ray (see Figure 5.9 (a)). The spectrum shows 416 keV, 430 keV and 437 keV new direct transitions and 511 keV, 678 keV, 766 keV, 846 keV and 853 keV new cross-over transitions of Band 2.

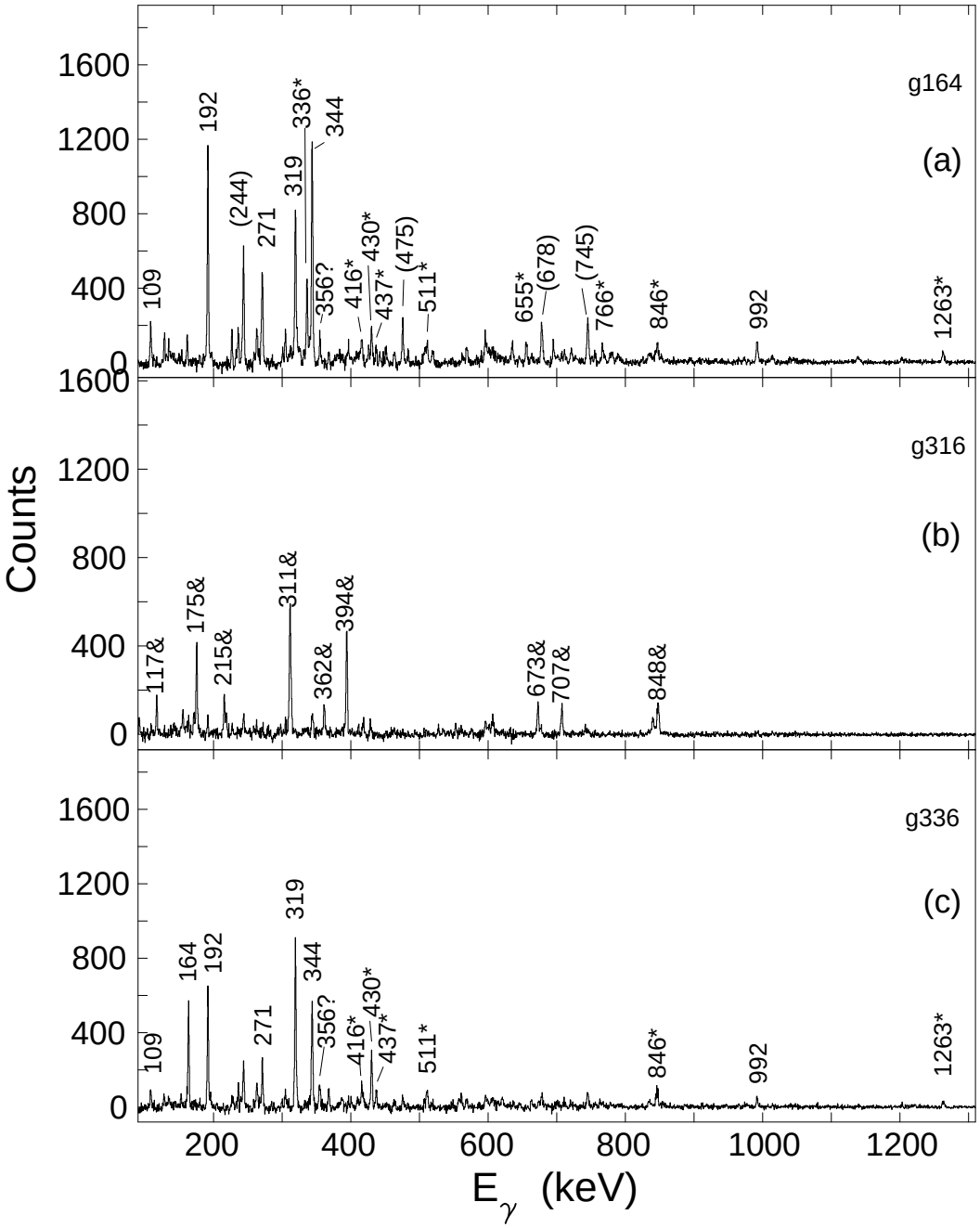

Figure 5.9: The coincidence spectrum obtained by setting a gate on 164 keV tranition panel (a) shows most of the transitions of Band 2 in ^{196}Tl. The new transitions in this band are labelled with symbol $*$. The 316 keV transition previously placed in Band 2 of ^{196}Tl is not seen in the spectrum. A gate set on the 316 keV panel (b) does not show any ^{196}Tl transitions, it rather shows the transitions of ^{195}Tl labelled with symbol &. A gate set on 336 keV panel (c) shows most of transitions of Band 2 and the links 992 keV and 1263 keV are also seen. The transitions placed in parenthesis are transitions of Band 3 in ^{196}Tl. The transitions labelled with ? could not be found in any residual nuclei.

The 1263 keV new link to Band 1 is also seen. These are labelled with $*$ in the spectrum. Gating back on these new transitions, Band 2 transitions are seen. A spectrum gated on a cross-over 846 keV (Figure 5.10 (b)), shows the 164 keV and 192 keV known peaks of Band 2 and 437 keV, 511 keV and 655 keV peaks of new transitions in this band. the 416 keV and 430 keV parallel decay transitions are not seen in the spectrum as expected. Thus the 848 keV is indeed a cross-over transition of Band 2. A spectrum gated on 853 keV (Figure 5.10 (c)) shows Band 2 transition peaks but 437 keV and 416 keV parallel transitions peaks are not seen as expected. Thus the 853 keV is a cross-over transition member of Band 2 and was placed there. Other new observed cross-over transitions are 511 keV, 655 keV 766 keV which are observed in the 164 keV gate.

Two new links of 755 keV and 1263 keV transitions from Band 2 to Band 1 were found in this work. The 755 keV weak transition links the(12^-) level of Band 2 to the $(12)^-$ level of Band 1 and 1263 keV links Band 2 from the (12^-) level to the $(10)^-$ level of Band 1. These links were observed as follows: A gate set on 164 keV (Figure 5.9 (a)) shows a clear peak of 1263 keV but the 755 keV peak could not be seen because it is very weak and can not be resolved from the background. Gating on 1263 keV in turn (Figure 5.11 (c)), the known transitions 164 keV, 192 keV, 319 keV and 336 keV of Band 2 together with transitions of Band 1 below the $(10)^-$ level (108 keV and 344 keV) are also seen. The 1263 keV peak is also seen in the 344 keV gate of Figure 5.4 and in most gates of Band 2 transitions. Further 271 keV + 992 keV = 1263 keV. Therefore the 1263 keV is most likely a cross-over of 271 keV and 992 keV and was placed there. The new 755 keV transition could not be resolved from the background. However, a gate set on 755 keV (Figure 5.11 (a)) shows transitions of Band 2 and the established transitions of Band 1 below the $(12)^-$ level. Further 755 keV + 236 keV = 991 keV. It is most likely that the 992 keV crosses over the 755 keV and 236 keV transitions. Consequently 755 keV is most likely another link of Band 2 to Band 1.

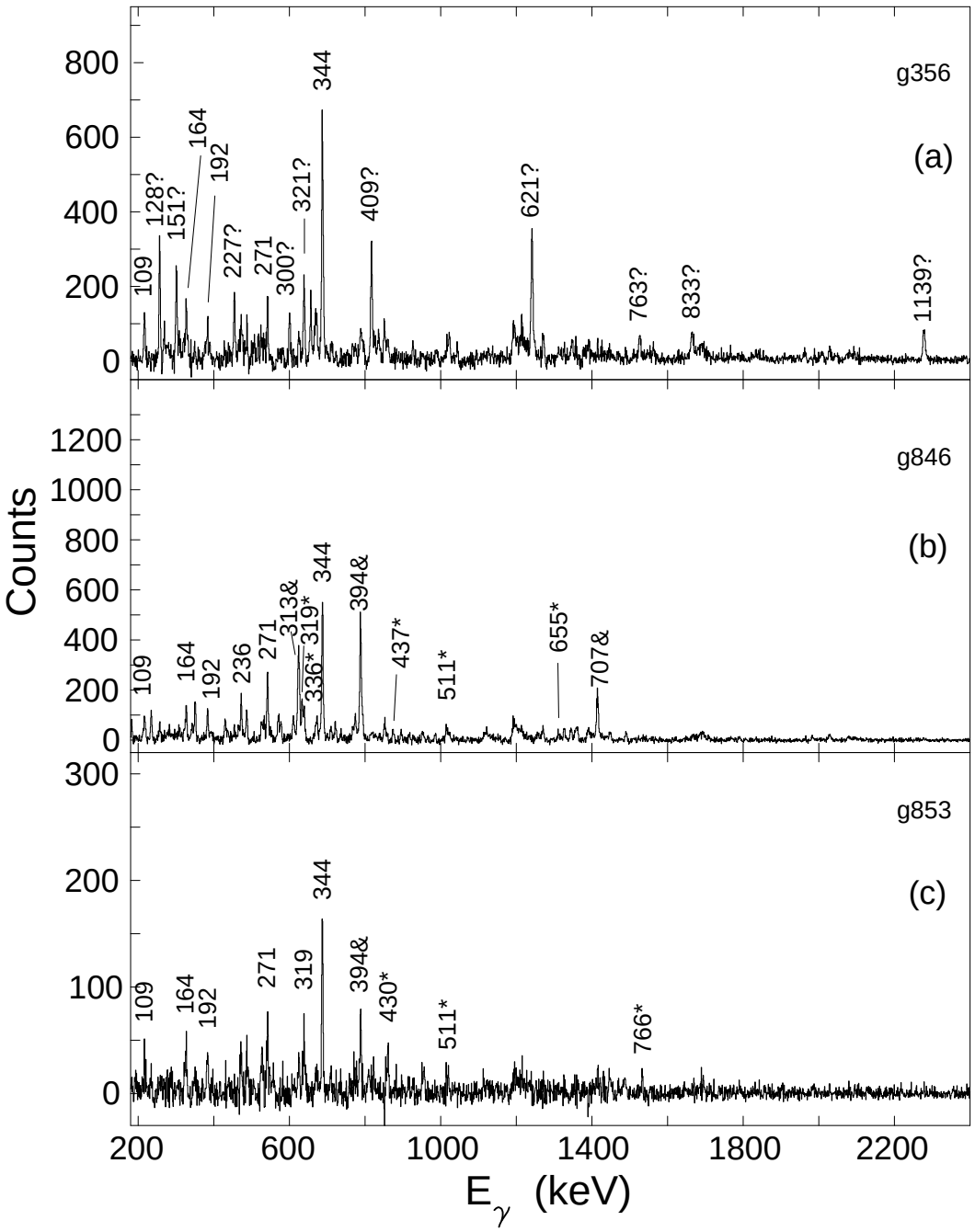

Figure 5.10: Panel (a) shows a spectrum gated on 356 keV transition previously placed parallel to 164 keV and 192 keV as tentative in Band 2 of ^{196}Tl. This spectrum shows most of transitions (labelled with ?) which could not be found in any residual nuclei. Further the presence of 164 keV and 192 keV transitions in the spectrum is unexpected. Thus the 356 keV transition does not show any evidence to be placed there. A gate set on the 846 keV panel (b) and 853 keV panel (c) new transitions, show the known and new transitions (labelled with $*$) of Band 2. The peaks labelled with symbols & are contaminants from^{195}Tl.

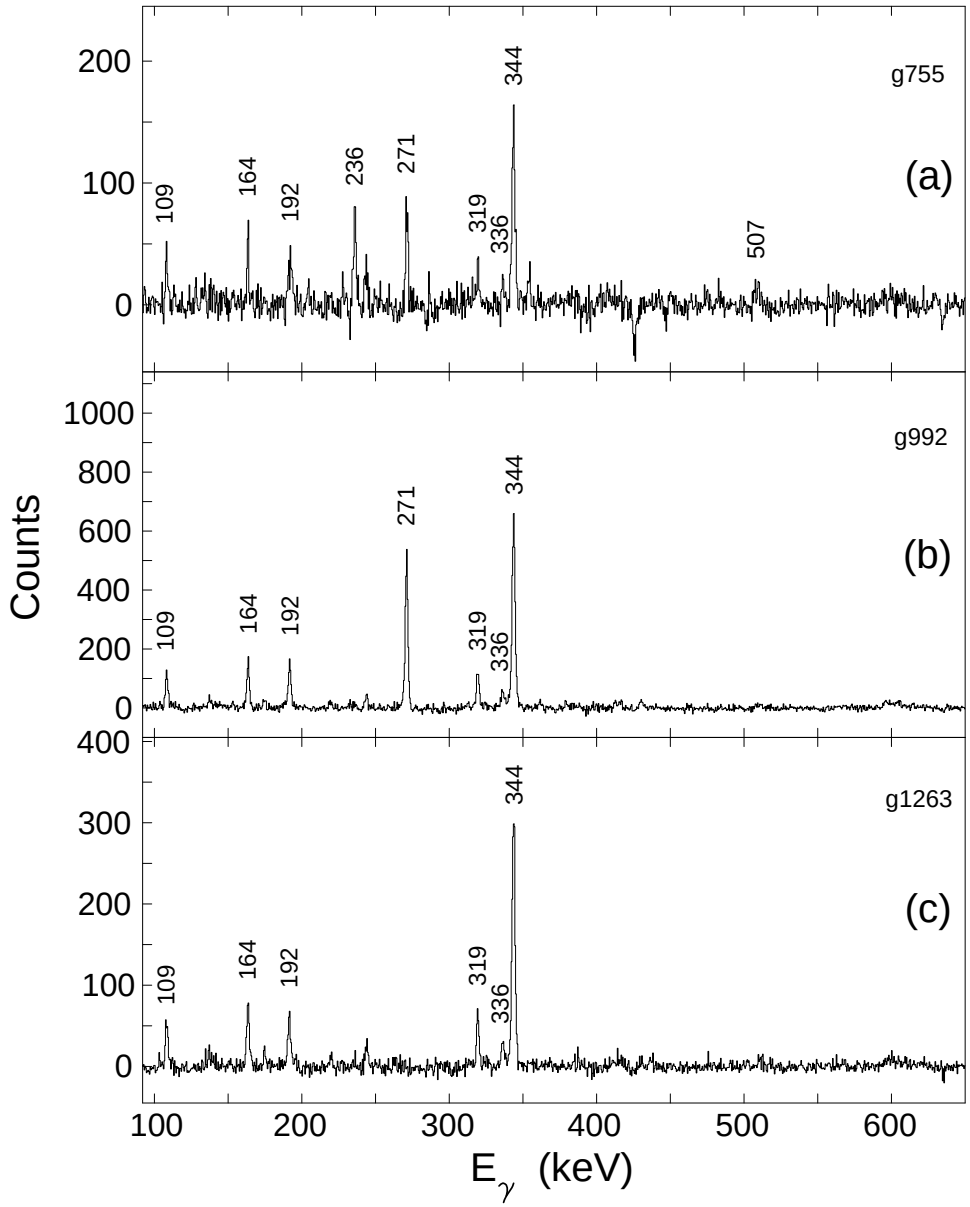

Figure 5.11: Panel (a), (b) and (c) show the coincidence spectra obtained by setting the gates on the 755 keV, 992 keV and 1263 keV respectively. These transitions link Band 2 to Band 1. Note the similarity of spectra, except the presence of 236 keV and 507 keV peaks in the 755 keV gate panel (a) and the absence of the 271 keV in the 1263 keV gate panel (c) as expected.

5.1.4 Band 3

Band 3 structure was established in the previous work up to an excitation energy of 1828 keV (with respect to the 7^+ isomer). It consisted of 5 direct γ-ray transitions in cascade, one tentative and 3 cross-over transitions (Figure 5.2). In the present work we have confirmed the established transitions and the tentative 270 keV was confirmed too. We have observed new transitions of 137 keV, 219 keV, 113 keV and a tentative 635 keV $\Delta I = 2$ cross-over was observed to decay parallel to the 161 keV and 475 keV transitions. With these observations, Band 3 was extended up to an excitation energy of 2297 keV.

A summed gate of 244 + 161 + 475 keV (Figure 5.12 (a)) shows the known γ-ray transitions of Band 3, the previous tentative 270 keV and new peaks of 137 keV, 219 keV and 113 keV (labelled with $*$). The single gated spectra on 137 keV and 219 keV shown in Figure 5.12 (b) and (c) respectively show the known 244 keV, 161 keV, 475 keV, 745 keV, 721 keV, 678 keV, 227 keV and the previous tentative 270 keV γ-rays. From the above observations, it is evident that the tentative 270 keV transition is present in this band. New peaks of 137 keV, 219 keV and 113 keV were observed in any gated transition of Band 3, and are most likely new transitions of this band. Thus, these three transitions were placed at the top of Band 3 based on their coincidence intensity. As no cross-over $\Delta I = 2$ transition was observed among these γ-rays, the order of their placement is tentative.

The 636 keV transition was added as a tentative $\Delta I = 2$ cross-over transition decaying parallel to the 161 keV and 475 keV transitions in this band as follows: in the summed gates of 244 + 161 + 475 keV spectrum shown in Figure 5.12 (a) the 636 keV peak is observed. Gating on the 636 keV peak in turn, the strong peaks of the ^{196}Hg nucleus and small peaks of Band 3 transitions are observed. This is because the ^{196}Hg nucleus has a strong 635 keV in its low-lying transitions. Gating on 636 keV very close to 635 keV, strong peaks of ^{196}Hg are seen. Thus the 636 keV is not a good gate. The gates set on the 161 keV and 475 keV which decay parallel to the 636 keV, see the 636 keV peak which is

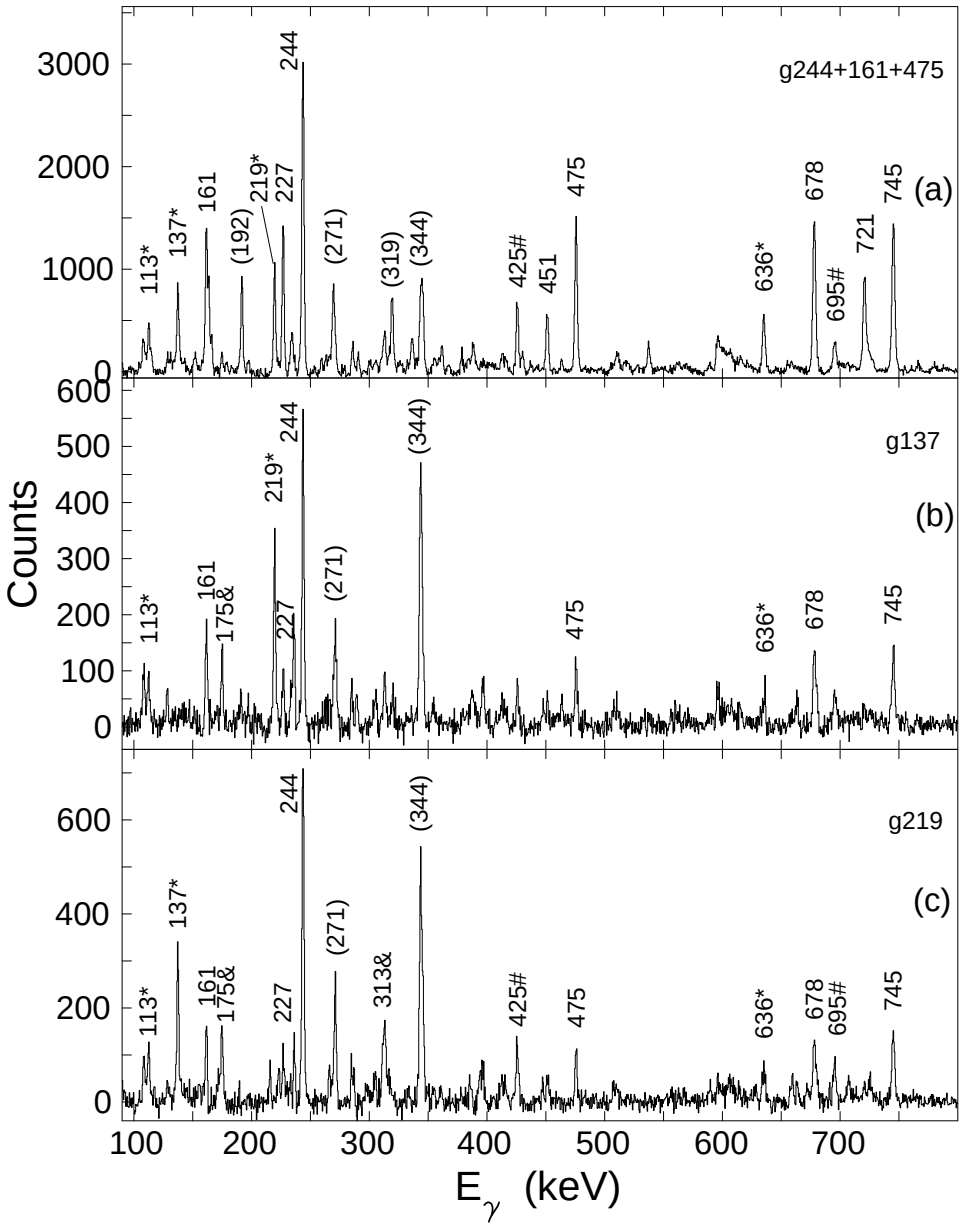

Figure 5.12: Panel (a) shows a spectrum gated on the 244 keV transition of Band 3. The known transitions of Band 3 and new transitions labelled with $*$ are clearly seen. Gating on the 137 keV and 219 keV transitions shown in panel (b) and (c) respectively, the known transitions of Band 3 can be seen. The transitions for which the energies are in parenthesis belong to Band 1 or Band 2 of ^{196}Tl. The peaks labelled with & and # are contaminants from ^{195}Tl and ^{196}Hg residual nuclei.

unexpected. It is not clear if the 636 keV transition is present in Band 3 or if it is just a contaminant from the ^{196}Hg nucleus. As the 244 keV gate sees the 636 keV and also 161 keV + 475 keV = 636 keV, it is possible that a weak 636 keV cross-over exists in Band 3 but is obscured by a strong 635 keV transition of the ^{196}Hg nucleus. Therefore the 636 keV transition was placed as tentative in Band 3.

5.2 DCO Measurements

To determine the multipolarities of new transitions, the *DCO* ratios (R_{DCO}) defined in Eq. (4.5) were measured using the known stretched $E2$ transitions as gates. The R_{DCO} for a number of transitions with known stretched $E2$ multipolarities were measured to provide the reference values for the current detector configuration. The theoretical R_{DCO} values were calculated using the code *DCOplot* [46], and were compared to the measured R_{DCO} values in order to determine the multipolarity of transitions. The *DCOplot* code is based on the theoretical formalism described in [50]. The obtained average values of $R_{DCO}(E2) = 1.08 \pm 0.12$ and $R_{DCO}(E1) = 0.70 \pm 0.07$ are very similar to the theoretical calculated values of $R_{DCO}(E2) = 1.0$ and $R_{DCO}(E1) = 0.69$ for the current detector configuration.

Figure 5.13 shows the plot of the measured R_{DCO} values for known and new transitions when a gate was set on a stretched quadrupole transition. One can notice that the stretched $\Delta I = 2$ cross over transitions tend to cluster around the R_{DCO} value of 1 and the $\Delta I = 1$ direct transitions tend to cluster around the R_{DCO} value of 0.69.

For transitions that were not in coincidence with any $E2$ transition or if the $E2$ was too weak to use as a gate, *DCO* ratios were measured by gating on a known stretched dipole ($E1$) transition. The average measured values of $R_{DCO}(E1) = 0.98 \pm 0.05$ and $R_{DCO}(E2) = 1.52 \pm 0.06$ are similar to the calculated theoretical values of $R_{DCO}(E1) = 1.0$ and $R_{DCO}(E2) = 1.44$. The graph is shown in Figure 5.14 where it can be seen that $\Delta I = 2$ cross-over transitions tend to cluster around the R_{DCO} values of 1.5 while $\Delta I = 1$ direct transitions tend to cluster around the R_{DCO} values of 1.0.

From the figure, it can be seen that the R_{DCO} values of new transitions have large uncertainties compared to those of known established transitions. This is because the new transitions are very weak compared to the known strong transitions of Band 1, and therefore it was necessary to calculate the theoretical R_{DCO} predictions to compare with the measured values in an attempt to deduce the multipolarities of the new transitions. When

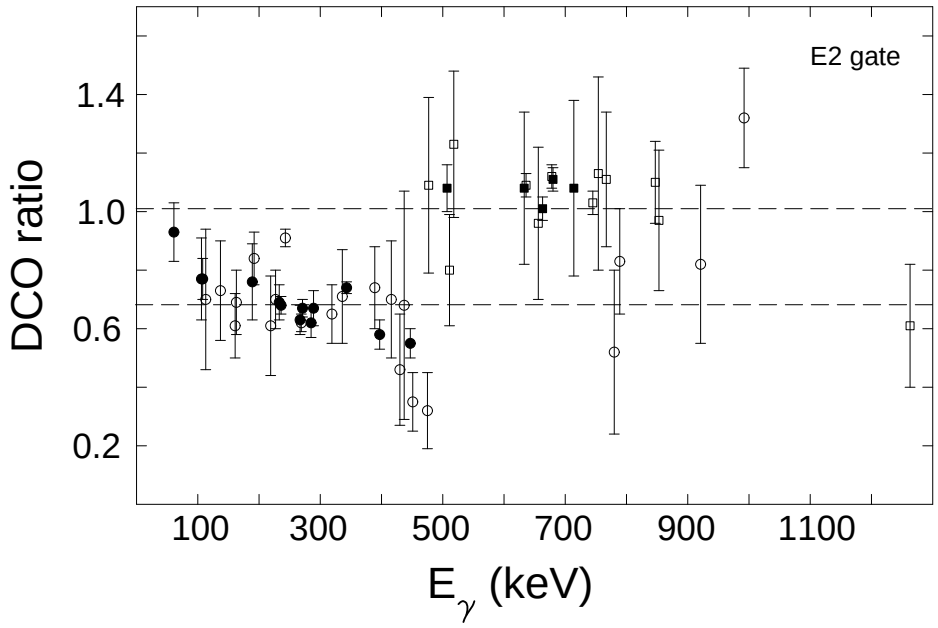

Figure 5.13: The R_{DCO} values as a function of energy for transitions in ^{196}Tl. The gates were set on the known stretched $E2$ transitions. Filled symbols indicate previously assigned transitions while open symbols indicate newly assigned transitions. The circle symbols denote stretched $\Delta I = 1$ while square symbols denote stretched $\Delta I = 2$. The dashed lines indicate the average of previous assignments for stretched $\Delta I = 1$ and stretched $\Delta I = 2$ used as references in the assignment of new transitions.

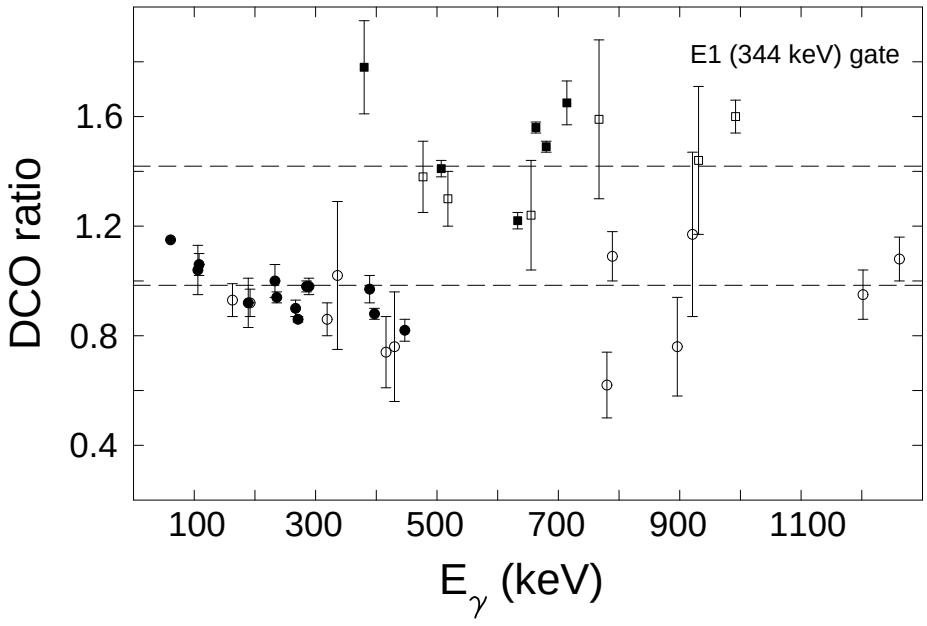

Figure 5.14: The R_{DCO} values as a function of energy for transitions in ^{196}Tl. The gate was set on a stretched $E1$ (344 keV) transition. Filled symbols indicate previously assigned transitions while open symbols indicate newly assigned transitions. The circle symbols denote stretched $\Delta I = 1$ while square symbols denote stretched $\Delta I = 2$. The dashed lines indicate the average of previous assignments for stretched $\Delta I = 1$ and stretched $\Delta I = 2$ used as references in the assignment of new transitions.

performing the calculations with the code PACE4, a deorientation parameter $\sigma/I = 0.35$ and oblate alignment were assumed, and the average azimuthal angle between clover detectors was $\Delta\phi = 45°$. The graphs of measured and calculated R_{DCO} values are plotted for most new transitions and are used in assigning spins and parities for new levels.

5.3 Linear polarization measurements

The linear polarization measurements are used to deduce the electric and magnetic character of γ-ray transitions. When the multipolarity of a transition is combined with the electric or magnetic character of the transition, the spin and parity of a new level can be assigned if it decays to a level of known spin and parity. The linear polarization measurements were performed following Eq. (4.7) which is defined in section 4.9. Since the linear polarization measurements do not depend on the multipolarity of the gate, the A_P values were determined using stretched $E2$ or mixed $M1/E2$ transitions as gates and the results are given in Figure 5.15.

5.4 Spin and parity assignments

In this work the spin-parity was assigned to the new levels and to the established levels of Band 2 and Band 3 which were not previously assigned. The spin-parity assignment was performed using the deduced multipolarities and character of linking transitions to the levels for which the spin-parity was known. The theoretical DCO ratios and theoretical polarization values were calculated for important transitions to compare with the measured values when assigning spin and parity to levels.

5.4.1 Band 1

Band 1 was assigned spin-parity in the previous work up to a tentative spin of $(20^- + I_0)$. In this work the labels of spins for levels above the 8^- level are put in parenthesis to

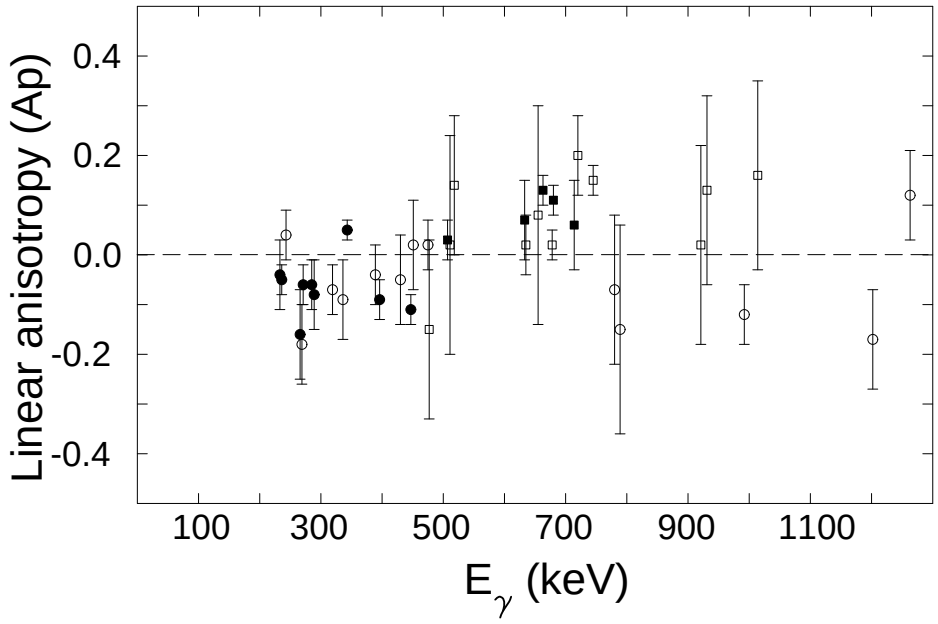

Figure 5.15: The linear polarization anisotropy (A_P) values as function of transition energy in the ^{196}Tl nucleus. Positive values are stretched electric unstretched magnetic transitions and negative values are stretched magnetic/unstretched electric transitions. Filled symbols are previously assigned transitions while open symbols are newly assigned transitions. Circle symbols denote stretched $\Delta I = 1$ and square symbols denote stretched $\Delta I = 2$

.

account for an unknown spin offset I_0 as suggested by Kreiner *et al.* [7]. The information about γ-ray energies, the deduced multipolarities and the spin-parity assigned to levels of Band 1 are summarised in Table 5.1. The assignments of levels in Band 1 were found to be consistent with the previous assignments and in the following we will concentrate on the newly assigned levels.

The (3236) keV level decays to the (3129) keV $(19)^-$ level via a 106 keV transition. The measured $R_{DCO}(106) = 0.77(14)$ value from a quadrupole gate is consistent with a $\Delta I = 1$ interpretation. The linear polarization of this transition could not be measured since the linear polarisation needs substantial Compton scatters which doesn't happen for E $\simeq$ 100 keV. As the 106 keV transition is a continuation of the rotational band of Band 1, the $M1/E2$ assignment seems more likely than $E2$. With the likely $M1/E2$ interpretation given to the 106 keV γ-ray, the level of 3236 keV was tentatively assigned spin and parity $I^\pi = (20)^-$.

The (3625) keV state decays to the (3236) keV $(20)^-$ level via a 389 keV transition. The measured $R_{DCO}(389) = 0.74(14)$ value with an $E2$ gate, is inconsistent with the $\Delta I = 2$ interpretation which will give a value close to 1. The theoretical calculated $R_{DCO}(389)$ values for $\Delta I = 0$ and $\Delta I = 1$ interpretations are shown in panel (a) of Figure 5.16. It can be seen that the $\Delta I = 1$ is more likely than the $\Delta I = 0$ interpretation. Further, the measured linear polarisation $A_P(389)$ = -0.04(6) agrees with the calculated value $A_P(389)$ = -0.041 for mixed $M1/E2$ more than the $\pm$0.15 value for $\Delta I = 0$ predictions. As result, the 389 keV is most likely a mixed $M1/E2$ transition and therefore the 3625 keV level was tentatively assigned spin and parity $I^\pi = (21)^-$.

The new cross-over transitions of 518 keV and 478 keV were observed to connect $(17)^-$ to $(15)^-$ and $(19)^-$ to $(17)^-$ levels of Band 1 respectively. The respective measured R_{DCO} values of 1.23(25) and 1.09(30) respectively from a quadrupole gate, are consistent with $E2$ interpretations. The A_P values of 0.14(14) and -0.15(18) are not statistically significant. As each of these transitions crosses over to two established stretched $\Delta I = 1$

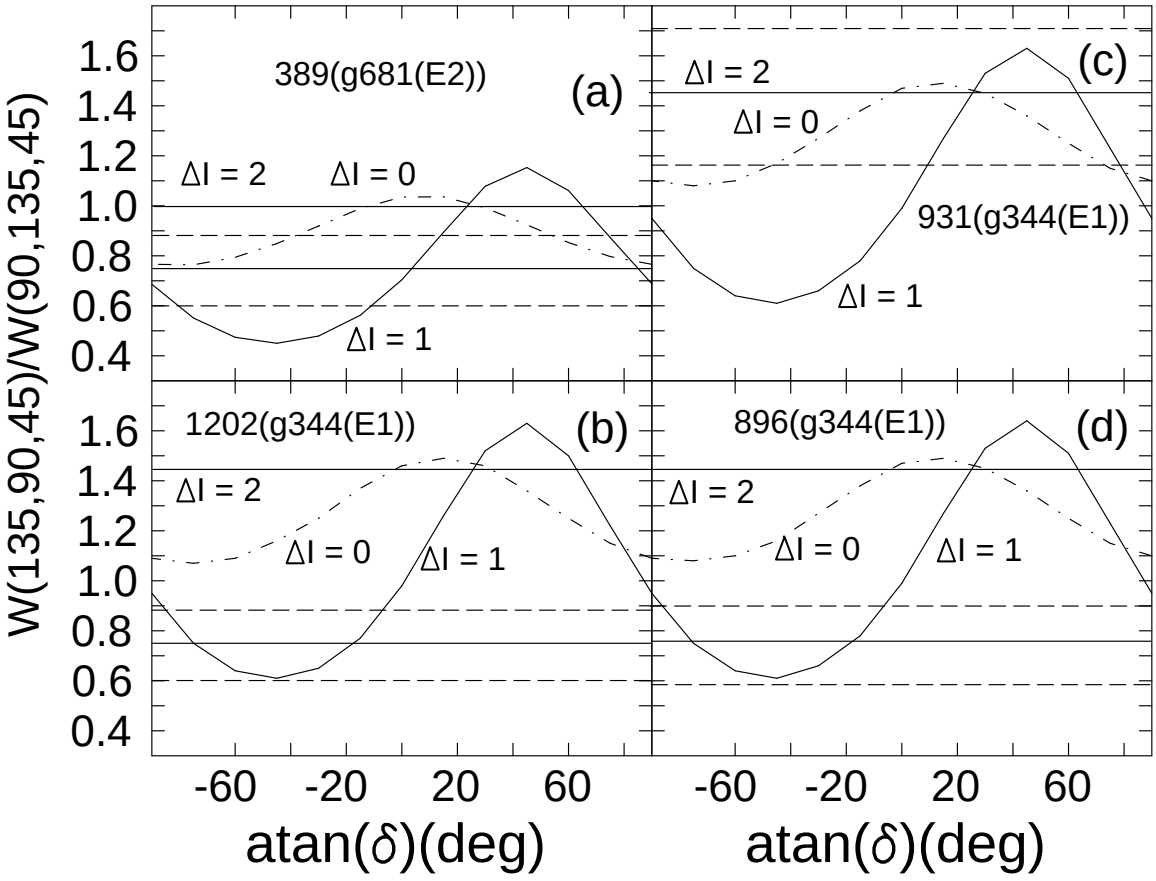

Figure 5.16: Calculated values of R_{DCO} as function of the mixing ratio δ. The curves correspond to $\Delta I = 0$ (broken lines curves) and $\Delta I = 1$ (continuous line curves) transitions. The measured R_{DCO} values (solid lines) and uncertainty (broken lines) for each transition are given on the relevant panel which gives also the γ-ray energy (keV), the energy and the character of the gate.

Table 5.1: *γ-ray energies, DCO ratios, linear polarization, and spin-parity assignment for levels in Band 1.*

E_γ(keV)	E^i_{ex}(keV)	$I^\pi_i \rightarrow I^\pi_f$	Gate	R_{DCO}	A_P	Deduced Multipolarity
344	344	$8^- \rightarrow 7^+$	$E2$	0.74(2)	0.05(2)	$E1$
61	(405)	$(9)^- \rightarrow 8^-$	$E2$	0.93(10)	-	$M1+E2$
109	(514)	$(10)^- \rightarrow (9)^-$	$E2$	0.77(7)	-	$M1+E2$
380	(785)	$(11)^- \rightarrow (9)^-$	$E2$	-	-	$E2$
271	(785)	$(11)^- \rightarrow (10)^-$	$E2$	0.67(3)	-0.06(4)	$M1$
507	(1022)	$(12)^- \rightarrow (10)^-$	$E2$	1.08(8)	0.03(4)	$E2$
236	(1022)	$(12)^- \rightarrow (11)^-$	$E2$	0.68(3)	-0.05(3)	$M1$
633	(1419)	$(13)^- \rightarrow (11)^-$	$E2$	1.08(26)	0.07(8)	$E2$
397	(1419)	$(13)^- \rightarrow (12)^-$	$E2$	0.58(5)	-0.09(4)	$M1$
664	(1685)	$(14)^- \rightarrow (12)^-$	$E2$	1.01(4)	0.13(3)	$E2$
266	(1685)	$(14)^- \rightarrow (13)^-$	$E2$	0.63(5)	-0.16(9)	$M1$
714	(2133)	$(15)^- \rightarrow (13)^-$	$E2$	1.08(30)	0.06(9)	$E2$
448	(2133)	$(15)^- \rightarrow (14)^-$	$E2$	0.55(5)	-0.11(3)	$M1$
681	(2366)	$(16)^- \rightarrow (14)^-$	$E2$	1.11(4)	0.11(3)	$E2$
233	(2366)	$(16)^- \rightarrow (15)^-$	$E2$	0.69(6)	-0.04(7)	$M1$
518	(2652)	$(17)^- \rightarrow (15)^-$	$E2$	1.23(25)	0.14(14)	$E2$
285	(2652)	$(17)^- \rightarrow (16)^-$	$E2$	0.62(5)	-0.06(5)	$M1$
289	(2940)	$(18)^- \rightarrow (17)^-$	$E2$	0.67(6)	-0.08(7)	$M1$
478	(3129)	$(19)^- \rightarrow (17)^-$	$E2$	1.09(30)	-0.15(18)	$E2$
188	(3129)	$(19)^- \rightarrow (18)^-$	$E2$	0.76(13)	-	$M1+E2$
106	(3236)	$(20)^- \rightarrow (19)^-$	$E2$	0.77(14)	-	$M1+E2$
389	(3625)	$(21)^- \rightarrow (20)^-$	$E2$	0.74(14)	-0.04(6)	$M1+E2$

transitions (Figure 5.2), it is clear that these two γ-rays are $E2$ cross over transitions of Band 1 and were placed there.

5.4.2 Energy levels decaying to Band 1

Levels of "group A " decay to levels of Band 1 via 781 keV, 789 keV, 827 keV, 896 keV, 921 keV, 931 keV and 1202 keV γ-rays transitions. The observation of these transitions was discussed in the previous section. These transitions are very weak and their *DCO* ratios measurements have large uncertainties. The deduced γ-ray multipolarities and assigned

spin and parity of levels in "group A " are summarized in Table 5.2.

Table 5.2: *γ-ray energies, DCO ratios, linear polarization, and spin-parity assignment for levels decaying to Band 1.*

E_γ(keV)	E^i_{ex}(keV)	$I^\pi_i \rightarrow I^\pi_f$	Gate	R_{DCO}	A_P	Deduced Multipolarity
1202	(1716)	$(11^-) \rightarrow (10)^-$	$E1$	0.74(14)	-0.17(10)	$M1+E2$
931	(1716)	$(11^-) \rightarrow (11)^-$	$E1$	1.44(27)	0.13(19)	unstretched $M1$
896	(1681)	$(12)^- \rightarrow (11)^-$	$E1$	0.76(18)	-	$M1+E2$
781	(1803)	$(13)^- \rightarrow (12)^-$	$E2$	0.52(28)	-0.07(15)	$M1+E2$
921	(2606)	- $\rightarrow (14)^-$	$E2$	0.82(27)	-0.02(20)	-
827	(2960)	- $\rightarrow (15)^-$	$E2$	-	-	-
789	(3440)	- $\rightarrow (16)^-$	$E2$	0.83(18)	-0.15(21)	-

The new level of (1716) keV decays to the (785) keV, $(11)^-$ and to the (514) keV, $(10)^-$ levels of Band 1 via 931 keV and 1202 keV γ-rays respectively. The measured R_{DCO} values for these γ-rays with the $E1$ gate are 1.44(27) and 0.74(14) respectively. The two values are inconsistent with a stretched $\Delta I = 1$ interpretation which will give a value close to 1. The $R_{DCO}(931)$ and $R_{DCO}(1202)$ measured values are compared with the theoretical predictions for the remaining possible interpretations of $\Delta I = 0$, mixed $\Delta I = 1$ and stretched $\Delta I = 2$, plotted in Figure 5.16 panel (b) and panel (c) respectively. It can be seen from the figure that $R_{DCO}(931)$ is consistent with the three interpretations. On the other hand, the measured $R_{DCO}(1202)$ value is consistent with only the $\Delta I = 1$ interpretation. With $\Delta I = 0$ and $\Delta I = 2$ ruled out, the 1202 keV is likely to be a mixed $M1/E2$ or an $E1$ transition. As the 1202 keV crosses over the 931 keV and the established 271 keV ($M1/E2$), the possible character for 1202 keV seems to be more likely a mixed $M1/E2$. This implies also that the 931 keV γ-ray should have the multipolarity of $\Delta I = 0$. Further the measured polarization $A_P(1202)$ = -0.17(10) is consistent with the theoretical value of -0.007 for a mixed $M1/E2$ interpretation. As this level feeds the tentative $(10)^-$ level, the (1716) keV level was tentatively assigned $I^\pi = (11)^-$.

The (1681) keV level decays to the (785) keV, $(11)^-$ of Band 1 via a 896 keV transition.

The measured $R_{DCO}(896) = 0.76(18)$ value from a stretched $E1$ gate, is inconsistent with a stretched $\Delta I = 2$ interpretation which will give a value close to 1.44. With $\Delta I = 2$ ruled out, the measured and the calculated $R_{DCO}(896)$ are compared for two remaining interpretations $\Delta I = 0$ and $\Delta I = 1$. The results are plotted in panel (d) of Figure 5.16 where it can be seen that the measured $R_{DCO}(896)$ is consistent with only the $\Delta = 1$ interpretation and only if the transition has a substantial quadrupole admixture, *viz.* $M1/E2$. With a mixed $M1/E2$ interpretation of the 896 keV γ-ray, the (1681) keV level was assigned $I^{\pi} = (12)^{-}$.

The (1803) keV level decays to the (1022) keV, $(12)^{-}$ level of Band 1 via a 781 keV transition. The measured $R_{DCO}(781) = 0.52(28)$ with a quadrupole gate is inconsistent with a stretched quadrupole interpretation which gives a value close to 1. With $\Delta I = 2$ ruled out, the measured and the calculated $R_{DCO}(781)$ were compared for two remaining likely interpretations $\Delta I = 0$ and $\Delta I = 1$. The results are plotted in Figure 5.17 (a), where it can be seen that $R_{DCO}(781)$ is consistent with the $\Delta I = 1$ interpretation and only if the transition has a substantial quadrupole admixture, *viz.* $M1/E2$. Further, the measured polarization anisotropy value of -0.07(15) is consistent with both theoretical predictions of -0.014 for $M1/E2$ and 0.047 for an $E1$ interpretations. But the most likely interpretation is a mixed $M1/E2$ multipolarity. As result, the (1803) keV level feeding the $(12)^{-}$ level was assigned $I^{\pi} = (13)^{-}$.

The (2606) keV level decays to the (1685) keV, $(14)^{-}$ level via a 921 keV transition. The measured $R_{DCO}(921) = 0.82(27)$ with a quadrupole gate has a large uncertainty and is consistent with $\Delta I = 0$, $\Delta I = 1$ and $\Delta I = 2$ interpretations. The theoretical R_{DCO} predictions for these interpretations are compared to the measured value in Figure 5.17 (b). The plot does not resolve the three interpretations since all three interpretations are possible. Further the $A_P(921)$ measured value of 0.02(20) is consistent with the theoretical A_P values of -0.02 for mixed $M1/E2$, ± 0.10 for unstretched $\Delta I = 0$ and 0.07 for stretched $E2$ interpretations. As the multipolarity and character of the 921 keV transition could

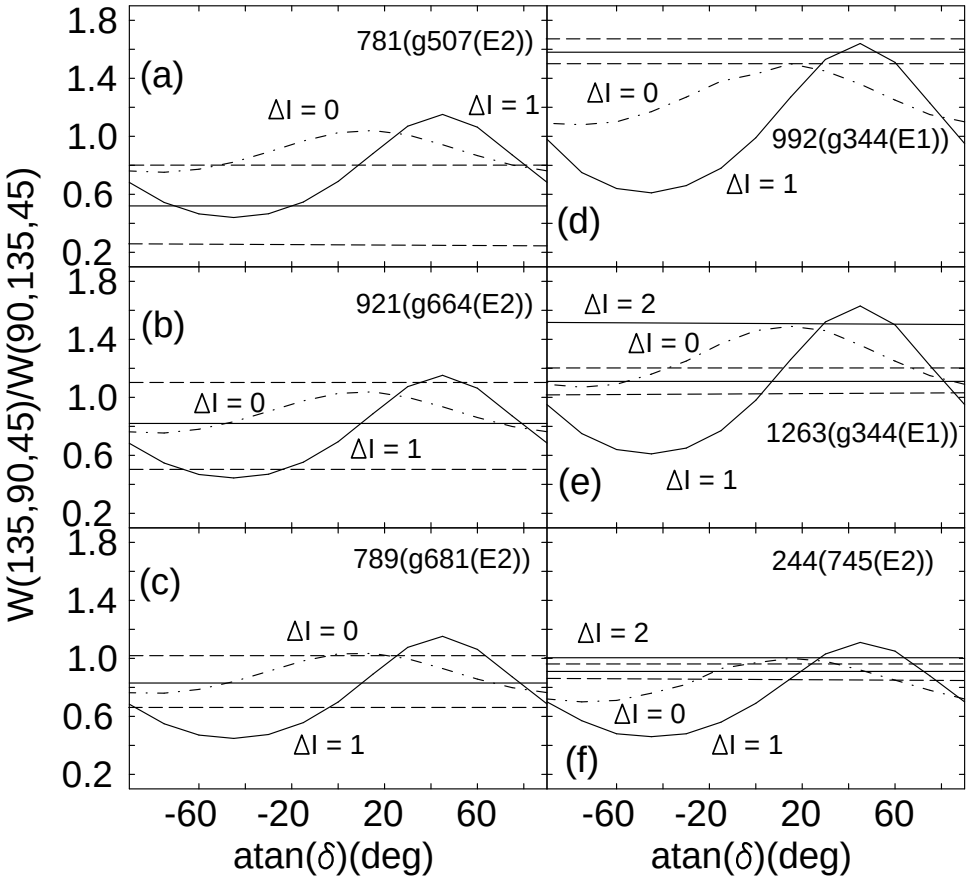

Figure 5.17: Calculated values of R_{DCO} as function of the mixing ratio δ. The curves correspond to $\Delta I = 0$ (broken line curves) and $\Delta I = 1$ (continuous line curves) transitions. The measured R_{DCO} values (solid line) and uncertainty (broken line) for each transition are given on the relevant panel which gives also the γ-ray energy (keV), the energy and the character of the gate.

not be determined, the (3155) keV level could not be assigned spin and parity.

A tentative (2960) keV level decays to the (2133) keV, $(15)^-$ level of Band 1 through a tentative 827 keV transition. The 827 keV transition is very weak and no measurement of *DCO* ratio and linear polarization was possible. As a result, the multipolarity of this tentative transition could not be determined and consequently the tentative (2606) keV level could not be assigned spin and parity.

The (3155) keV level decays to the (2366) keV, $(16)^-$ level of Band 1 via a 789 keV transition. The measured $R_{DCO}(789) = 0.83(18)$ with a quadrupole gate is consistent with $\Delta I = 0$, $\Delta I = 1$ and $\Delta I = 2$ interpretations. The measured R_{DCO} values compared to the predictions of the calculated value for these interpretations show that all three interpretations are possible (see Figure 5.17 (c)). Further the measured $A_P(789)$ = -0.15(21) value is consistent with theoretical predictions of -0.03 for $M1/E2$, ± 0.114 for $\Delta I = 0$ and 0.084 for stretched $E2$ interpretations. As the three interpretations can not be distinguished the 789 keV γ-ray could not be assigned. As a result, the (3155) keV level was not assigned spin and parity.

5.4.3 Band 2

Band 2 is assigned spin-parity for the first time in this work. The I^π assignment was performed following the determination of multipolarity and character of linking transitions to levels of Band 1 for which spin-parity are already known. Table 5.3 summarizes the information about the γ-ray energies of Band 2, the initial excitation energy of levels, the multipolarity and spin and parity assignment.

Band 2 is linked to Band 1 via three transitions of 755 keV (1777 keV $\rightarrow (11)^-$), 992 keV (1777 keV $\rightarrow (11)^-$) and 1263 keV (1777 keV $\rightarrow (10)^-$) as shown in Figure 5.2. The measured R_{DCO} for the two last transitions with an $E1$ (344 keV) gate are: 1.58(6) and 1.11(8) respectively. The R_{DCO} of 755 keV could not be measured because it was very weak. The measured $R_{DCO}(992) = 1.58(6)$ is inconsistent with the stretched $\Delta I = 1$

interpretation which will give a value close to 1. With stretched $\Delta I = 1$ ruled out, the remaining possible interpretations of $\Delta I = 0$, mixed $\Delta I = 1$ and stretched $\Delta I = 2$. The calculated values are compared with the measured $R_{DCO}(992)$ value in Figure 5.17 (d). From the figure one can see that only two interpretations of $\Delta I = 0$ and $\Delta I = 1$ are possible. Further, the measured linear polarization $A_p(992)$ = -0.12(6) value is consistent with the theoretical value of -0.114 for unstretched $E1$ but inconsistent with the value of -0.03 for mixed $M1/E2$ and positive value for stretched $E1$ interpretations. Further, the character of the 1263 keV transition would help us to know the 992 keV character since the two transitions depopulate the same level. The measured $R_{DCO}(1263) = 1.11(8)$ from an $E1$ gate, is consistent with a stretched $\Delta I = 1$ interpretation which has a value close to 1, and inconsistent with the stretched $E2$ which has a value close to 1.44. The theoretical $R_{DCO}(1263)$ for $\Delta I = 0$, mixed $\Delta I = 1$ and stretched $\Delta I = 2$ interpretations are plotted in Figure 5.17 (e). From the figure, one can see that only $\Delta I = 1$ interpretation is possible, *viz.* stretched $M1$ or mixed $M1/E2$ or stretched $E1$. The measured linear anisotropy $A_p(1263) = 0.17(6)$ is inconsistent with the $M1/E2$ and $M1$ characters which will give the value $A_P < 0$, but consistent with a stretched $E1$ character with a value > 0. As result, the only assignment of the (1777) keV level that can satisfy both characters of 992 keV and 1263 keV transitions, is the spin and parity of $I^\pi = (11)^+$.

As the band head of Band 2 was assigned spin and parity of $(11)^+$, it established the positive parity assignment of this band. The I^π assignment for transitions above the band head was facilitated by the establishment of stretched $\Delta I = 2$ cross-over transitions observed in this band. The measured R_{DCO} values for in-band transitions given in table 5.3 are consistent with stretched $\Delta I = 1$ and only if each transition has a substantial quadrupole admixture. The large uncertainties are due to the fact that this band is weak. The measured negative value of the polarization confirms the magnetic character assigned to the direct transitions. As a result these transitions were determined to be pure $M1$ or mixed $M1/E2$ transitions. The measured R_{DCO} close to 1 from an $E2$ gate for cross-over

Table 5.3: *γ-ray energies, DCO ratios, linear polarization, and spin-parity assignment for levels in Band 2.*

E_γ(keV)	E^i_{ex}(keV)	$I^\pi_i \rightarrow I^\pi_f$	gate	R_{DCO}	A_P	Deduced Multipolarity
1263	(1777)	$(11)^+ \rightarrow (10)^-$	$E1$	1.11(8)	0.17(6)	$E1$
992	(1777)	$(11)^+ \rightarrow (11)^-$	$E1$	1.58(6)	-0.12(6)	unstretched $E1$
755	(1777)	$(11)^+ \rightarrow (12)^-$	-	-	-	$E1$
164	(1941)	$(12)^+ \rightarrow (12)^+$	$E1$	0.93(6)	-	$M1$
192	(2133)	$(13)^+ \rightarrow (13)^-$	$E1$	0.92(5)	-	$M1$
511	(2452)	$(14)^+ \rightarrow (13)^-$	$E2$	0.80(19)	0.02(22)	$E2$
319	(2452)	$(14)^+ \rightarrow (14)^-$	$E1$	0.86(6)	-0.07(5)	$M1$
655	(2788)	$(15)^+ \rightarrow (14)^-$	$E2$	0.96(26)	0.08(22)	$E2$
336	(2788)	$(15)^+ \rightarrow (15)^-$	$E2$	0.71(16)	-0.09(8)	$M1 + E2$
766	(3218)	$(16)^+ \rightarrow (15)^-$	$E2$	1.11(23)	-	$E2$
430	(3218)	$(16)^+ \rightarrow (16)^-$	$E2$	0.46(19)	-0.01(15)	$M1 + E2$
846	(3634)	$(17)^+ \rightarrow (16)^-$	$E2$	1.10(14)	-	$E2$
416	(3634)	$(17)^+ \rightarrow (17)^-$	$E2$	0.70(20)	-0.05(19)	$M1 + E2$
853	(4071)	$(18)^+ \rightarrow (17)^-$	$E2$	0.97(24)	-	$E2$
437	(4071)	$(18)^+ \rightarrow (18)^-$	$E2$	0.68(30)	-	$M1 + E2$

$E2$ transitions in Band 2 and the positive A_P values (when possible) are consistent with the $E2$ transitions assignment. Therefore Band 2 was assigned negative parity with the highest observed spin of $(18)^+$.

5.4.4 Band 3

Band 3 is assigned I^π for the first time in this work. This band decays to the 7^+ isomer via 244 keV. The measured $R_{DCO}(244) = 0.91(3)$ with an $E2$ gate is inconsistent with a pure stretched $\Delta I = 1$ which will give a value close to 0.69. The measured R_{DCO} is compared to the calculated $R_{DCO}(244)$ values for $\Delta I = 0$, mixed $\Delta I = 1$ and stretched $\Delta I = 2$ interpretations as plotted in Figure 5.17 (f). One can see that the 0.91(3) value is inconsistent with a stretched $\Delta I = 2$ interpretation but consistent with $\Delta I = 0$ and mixed $\Delta I = 1$ interpretations. The measured $A_P(244) = 0.04(5)$ value indicates that 244 keV is most likely a mixed $M1/E2$ which gives a theoretical value of 0.04 and less

Table 5.4: *γ-ray energies, DCO ratios, linear polarization, and spin-parity assignment for levels in Band 3.*

E_γ(keV)	E^i_{ex}(keV)	$I^\pi_i \rightarrow I^\pi_f$	gate	R_{DCO}	A_P	Deduced Multipolarity
244	244	$(8^+) \rightarrow (7^+)$	$E2$	0.91(3)	0.00(5)	$M1+E2$
161	405	$(9^+) \rightarrow (8^+)$	$E2$	0.61(11)	-	$M1+E2$
635	880	$(10^+) \rightarrow (8^+)$	$E2$	1.09(4)	0.02(6)	$E2$
475	880	$(10^+) \rightarrow (9^+)$	$E2$	0.32(13)	0.02(5)	$M1+E2$
745	1150	$(11^+) \rightarrow (9^+)$	$E2$	1.03(4)	0.15(3)	$E2$
269	1150	$(11^+) \rightarrow (10^+)$	$E2$	0.62(3)	-0.18(8)	$M1+E2$
720	1601	$(12^+) \rightarrow (10^+)$	$E2$	-	0.20(8)	$E2$
451	1061	$(12^+) \rightarrow (11^+)$	$E2$	0.35(10)	0.02(9)	$M1+E2$
678	1828	$(13^+) \rightarrow (11^+)$	$E2$	1.11(23)	0.02(3)	$E2$
227	1828	$(13^+) \rightarrow (12^+)$	$E2$	0.70(10)	-	$M1+E2$
137	1965	$(14^+) \rightarrow (13^+)$	$E2$	0.73(17)	-	$M1+E2$
219	2184	$(15^+) \rightarrow (14^+)$	$E2$	0.61(17)	-	$M1+E2$
113	2297	$(16^+) \rightarrow (15^+)$	$E2$	0.70(24)	-	$M1+E2$

likely consistent with a $\Delta I = 0$ which gives a theoretical value of ± 0.6. Based on this the 244 keV transition is most likely a mixed $M1/E2$ but as $\Delta I = 0$ is also not excluded, the 244 keV level is tentatively assigned spin-parity of (8^+) since (7^+) can also be possible.

After tentatively assigning spin and parity of 8^+ to the band head of Band 3, the levels decaying above this level were consequently tentatively assigned spins of an upper limit (the spin could also be one unit less). The assignment for Band 2 was facilitated by observation of cross-over $E2$ transitions along with direct transitions in this band. The measured $0.32 < R_{DCO} < 0.73$ values for direct in-band transitions as shown in table 5.4, are consistent with a stretched $\Delta I = 1$ interpretation and only if each transition has a substantial quadrupole admixture. The positive values of A_P are consistent with the $M1/E2$ interpretation. The measured R_{DCO} values ~ 1 for the cross-over $E2$ transitions in this band with an $E2$ gate, and are consistent with the stretched $E2$ assignment. Further, the obtained positive values of polarization for these cross-over $E2$ transitions are consistent with pure stretched $E2$ transitions assignments. As a result, Band 3 is

tentatively assigned the I^{π} with positive parity up to $I^{+} = (16^{+})$.

Chapter 6

DISCUSSION AND CONCLUSION

This chapter provides the interpretation of the experimental data in relation to the theoretical predictions of the cranked shell model (CSM) and total Routhian surface (TRS) calculations. TRS calculations were performed by Pai *et al.* [1] and were used to determine the shape and the deformation of Band 1 in ^{196}Tl and are compared with those of similar bands in the neighbouring odd-odd Tl isotopes. The measured reduced transition probabilities ($B(M1)/B(E2)$) for Band 1 are compared to the theoretical predictions to determine the nuclear configuration of Band 1. The Routhians and alignment for Band 1 in ^{196}Tl are plotted as a function of angular frequency $\hbar\omega$ and are compared with those of neighboring nuclei in order to identify which quasi-nucleon orbital is involved in alignment. The configurations of Band 2 and 3 are not discussed because of the lack of data of some parameters such as g-factors and quadrupole deformation needed for theoretical calculations. These parameters may be obtained from lifetime measurements.

6.1 Configuration assignment of Band 1 in ^{196}Tl

The rotational band based on the 8^- state in ^{196}Tl was studied early in 1978 by Kreiner *et al.* [7] in the framework of a particle-plus-rotor model [11]. It was interpreted as being the coupling of a $h_{9/2}$ proton orbital with the $i_{13/2}$ neutron orbital, which are in turn

coupled to the oblate core rotor. The systematic similarities between the ground state bands of Tl isotopes such as ^{190,192,194,196,198}Tl indicate that these bands are based on the same intrinsic structure of $\pi h_{9/2} \otimes \nu i_{13/2}$ [1, 3, 7, 15]. In this section we want to prove the the configuration of Band 1 in ^{196}Tl by using the reduced transition probability ($B(M1)/B(E2)$) ratio method. The experimental $B(M1)/B(E2)$ values are compared with the calculated $B(M1)/B(E2)$ values for the most likely couplings of $\pi h_{9/2} \otimes \nu i_{13/2}$ and $\pi i_{13/2} \otimes \nu i_{13/2}$ near Fermi levels in the $A \sim 190$ mass region.

The experimental $B(M1)/B(E2)$ ratios are expressed according to the relation described in [6]:

$$\frac{B(M1)}{B(E2)} = 0.697 \frac{[E_\gamma(E2)]^5}{[E_\gamma(M1)]^3} \times \frac{1}{\lambda} \frac{1}{1+\delta^2} \left(\frac{\mu_N^2}{e^2 b^2}\right). \tag{6.1}$$

Here, λ is the branching ratio defined as:

$$\lambda = \frac{T_\gamma(\Delta I = 1)}{T_\gamma(\Delta I = 2)}, \tag{6.2}$$

where $T_\gamma(\Delta I = 2)$ and $T_\gamma(\Delta I = 1)$ are γ-ray intensities for $\Delta I = 2$ and $\Delta I = 1$ respectively, and δ is the $E2/M1$ mixing ratio for the $\Delta I = 1$ transitions. $E_\gamma(M1)$ and $E_\gamma(E2)$ are transition energies in units of MeV for $\Delta I = 1$ and $\Delta I = 2$ respectively. The relative intensities T_γ were extracted from the spectra gated on a transition just above the transitions of interest in the band, and the relative intensities were corrected with the detection efficiencies.

The theoretical $B(M1)$ and $B(E2)$ values were calculated using the Donau and Frauendorf formulas [51]:

$$B(M1) = \frac{3}{8\pi} [(g_p - g_R)A + (g_n + g_R)B]^2 \ \mu_N^2 \ , \tag{6.3}$$

where

$$A = (1 - \frac{K^2}{I^2})^{1/2} \Omega_p - i_p \frac{K}{I} \ , \tag{6.4}$$

and

$$B = (1 - \frac{K^2}{I^2})^{1/2}\Omega_n - i_n\frac{K}{I} \cdot \tag{6.5}$$

Here $g_{p(n)}$, $i_{p(n)}$ and $\Omega_{p(n)}$ are the g-factor, the alignment, and the angular momentum component on the symmetry axis of the proton and neutron respectively. The $B(E2)$ is expressed by [51]:

$$B(E2) = \frac{5}{32\pi}Q_0^2\cos^2(\gamma + 30^\circ) \times (1 - \frac{K}{I-1})^2\ (\mathrm{e^2b^2})\ , \tag{6.6}$$

where Q_0 is the quadrupole moment calculated [17] as:

$$Q_0 = \frac{3ZR^2\beta_2}{(5\pi)^{1/2}}\ (\mathrm{eb}) \cdot \tag{6.7}$$

The parameters used in the calculations are: $i_p = 2$ and $i_n = 6$ adopted from a $\pi\ h_{9/2}$ coupled band in the ^{195}Tl [13] and a $\nu\ i_{13/2}$ decoupled band in the ^{195}Hg [52]. The g_p-factor of 0.86 was taken from the $(\pi\ h_{9/2})_{9/2^-}$ state in the ^{195}Tl [13] and the g_n factor of -0.18 from the $(\nu\ i_{13/2})_{13/2^+}$ state in the ^{195}Hg [52]. The rotational gyromagnetic factor was assumed to be $g_R = Z/A = 0.4$. For the component K ($K = \mid \Omega_p \pm \Omega_n \mid$) in Eq. (6.6), we used values of 3, 4, 5 for $\pi\ h_{9/2} \otimes \nu\ i_{13/2}$ and 5, 6, 7 for the $\pi\ i_{13/2} \otimes \nu i_{13/2}$ configurations. Here the proton orbital $\pi h_{9/2}$ has Nilsson quantum number $[505]9/2^-$ which is the Fermi surface for protons in oblate deformation as indicated by Nilsson diagram of Figure 2.2 and the neutron orbital $\nu\ i_{1/2}$ has the Nilsson number $[660]1/2^+$ which is the Fermi surface for neutrons as indicated in Figure 2.1. The deformation parameters $\beta_2 = 0.15$ and $\gamma = -60^\circ$ were taken from the TRS calculation by Pai *et al.* [2]. The mixing ratio δ was assumed to be equal to zero ($\delta = 0$).

Figure 6.1 shows the plot of the measured $B(M1)/B(E2)$ values of Band 1 in ^{196}Tl before the bandcrossing with assumption of $\delta = 0$. From the graph it is observed that the calculated $B(M1)/B(E2)$ ratios corresponding to the $\pi i_{13/2} \otimes \nu i_{13/2}$ configuration

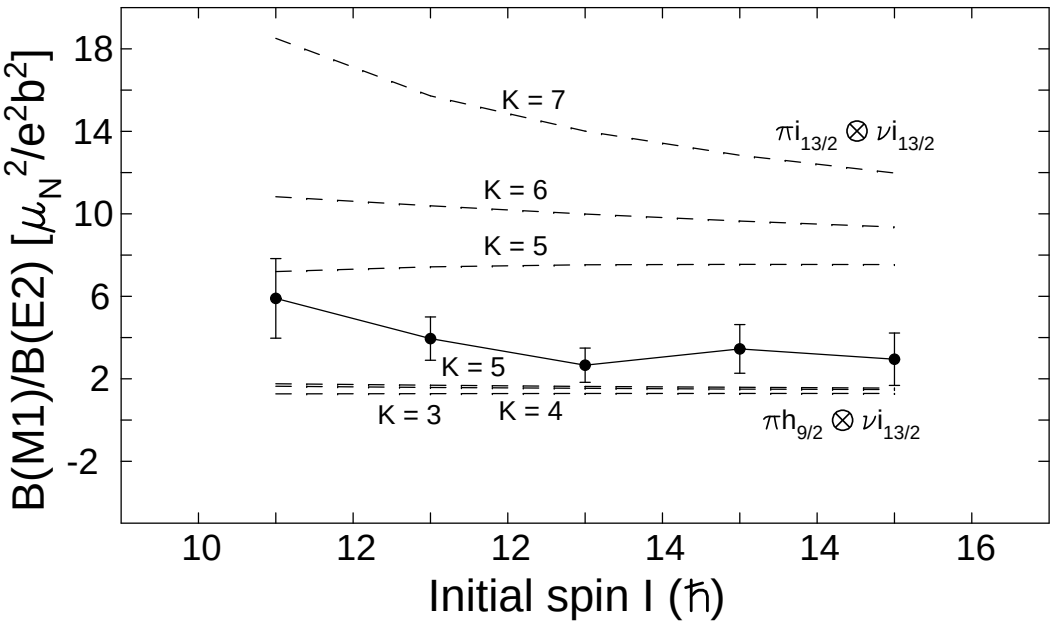

Figure 6.1: Experimental $B(M1)/B(E2)$ ratios (continuous line) as a function of initial spin I for Band 1 and theoretical predictions (dashed lines) for the $\pi\ h_{9/2}\ \otimes\ \nu\ i_{13/2}$ and $\pi\ i_{13/2}\ \otimes\ \nu\ i_{13/2}$ configurations assuming oblate deformation and mixing ratio $\delta = 0$.

are larger than the experimental values. This is true even for the lowest variable K of this configuration (for $K = 5$). This suggests that $\pi\ i_{13/2}\ \otimes\ \nu\ i_{13/2}$ is not a likely configuration of this band. On the other hand, it can be seen that the $B(M1)/B(E2)$ ratios for $\pi h_{9/2} \otimes \nu\, i_{13/2}$ are consistent with the experimental values. Therefore, $\pi h_{9/2} \otimes \nu\, i_{13/2}$ is the most likely configuration of the low-lying high spin states in the negative parity band, Band 1 of ^{196}Tl.

6.2 Bandcrossings and alignments of Band 1

To observe the bandcrossing and alignments of Band 1 of ^{196}Tl, the experimental excitation energies and spins had to be transformed into the rotating frame. The Harris parameters $\mathscr{I}_0 = 8.0\ \hbar^2\ \mathrm{MeV}^{-1}$ and $\mathscr{I}_1 = 40\ \hbar^4\ \mathrm{MeV}^{-3}$ were used. These parameters are the same parameters used in neighbouring $^{194,\ 198}$Tl [1, 15] and are derived in Ref. [53]. Figure 6.2 shows the alignment of Band 1 in ^{196}Tl, as a function of the rotational frequency $\hbar\,\omega$ together with those of the neighbouring odd-A ^{195}Tl isotope and ^{195}Hg isotone for comparison. It can be seen that the $\alpha = +1$ signature of Band 1 of ^{196}Tl has an initial alignment of 8 $\hbar$ which is equal to the sum of the $\alpha = +1/2$ signature alignment, $2\hbar$ of $^{195}_{81}$Tl [13] and the $\alpha = +1/2$ signature alignment, $6\hbar$ of $^{195}_{80}$Hg [5].

It can be seen from the figure that the alignments of ^{195}Tl and ^{195}Hg show the bandcrossings around 0.30 MeV and 0.25 MeV respectively. These bandcrossings were interpreted as due to the alignments of the pairs of $\nu\ i_{13/2}$ quasineutrons [2, 5]. However, the bandcrossing of ^{196}Tl is not observed since no sufficient experimental data are available. There is an upbend that starts to develop at around 0.30 MeV frequency which is higher than the bandcrossing frequencies of ^{195}Tl and ^{195}Hg as expected (see Figure 6.2). In ^{195}Tl and ^{195}Hg, the bandcrossings are interpreted as due to the alignments of the pairs of $\nu\ i_{13/2}$ quasineutrons [2, 5]. In ^{196}Tl, the AB quasineutron Routhian crossing is blocked and the bandcrossing is expected to occur at higher frequency. It is reported that the

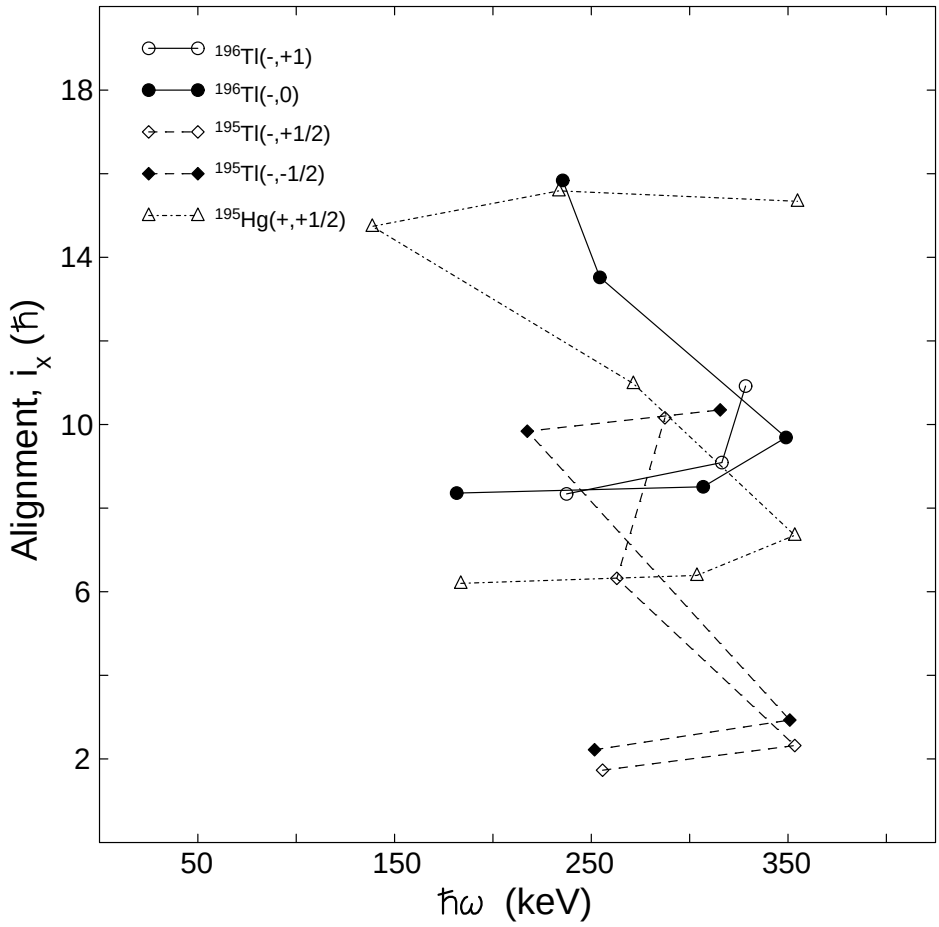

Figure 6.2: Alignment of Band 1 in ^{196}Tl compared to the corresponding band alignment in the ^{195}Tl isotope and ^{195}Hg isotone. It can be seen that Band 1 of ^{196}Tl has an initial alignment of 8 $\hbar$ which is equal to the sum of that of $2\hbar$ for ^{195}Tl and $6\hbar$ for ^{195}Hg. The symbol ^{196}Tl(-,+1) denotes the ground state band of ^{196}Tl with negative parity and signature +1.

proton alignment in the $A \simeq 190$ range nuclei, takes place at higher frequencies [2, 3, 5]. Thus it is most likely that the observed upbend in ^{196}Tl might be due to the alignment of the BC quasineutron Routhian. To fully characterise Band 1 of ^{196}Tl, the Cranked Shell Model (CSM) calculations [24] were needed to predict the properties of the band but the code of CSM was not available. It is also noted that the data for the full backbend of Band 1 in ^{196}Tl are not available. Therefore the population to higher spins of this band is necessary to fully understand it.

6.3 Routhians and kinematic moment of inertia for Band 1

The experimental Routhians and kinematic moment of inertia $\mathscr{I}^{(1)}$ for Band 1 in ^{196}Tl are plotted in Figure 6.3. The corresponding bands in neighbouring odd-odd isotopes ^{194}Tl and ^{198}Tl are also plotted for comparison. These consist of 2-quasiparticle $\pi\, h_{9/2} \otimes \nu\, i_{13/2}$ yrast bands observed in Ref.[1, 15]. The upper panel of Figure 6.3 shows the Routhians of the doubly-odd Tl isotopes ^{194}Tl, ^{196}Tl and ^{198}Tl as function of angular frequency. It is observed that the Routhians of these isotopes decrease with the increase of the angular frequency below the bandcrossing frequencies $\hbar\,\omega_c$. It is also observed that the Routhians increase with the neutron number. The latter effect is due to the neutron shell filling as the neutron number increases [28]. Another observed effect is that the three curves are exactly parallel to each other below the bandcrossing frequencies. This suggests that the 2-quasiparticle yrast bands in ^{194}Tl, ^{196}Tl and ^{198}Tl isotopes have the same intrinsic structure.

The kinematic moment of inertia $\mathscr{I}^{(1)}$ for ^{194}Tl, ^{196}Tl and ^{198}Tl isotopes are plotted in the lower panel of Figure 6.3 as a function of angular frequency. The fact that these moments of inertia are very similar suggests that these isotopes may have the same configuration and similar deformation. The bandcrossings for these nuclei are not fully

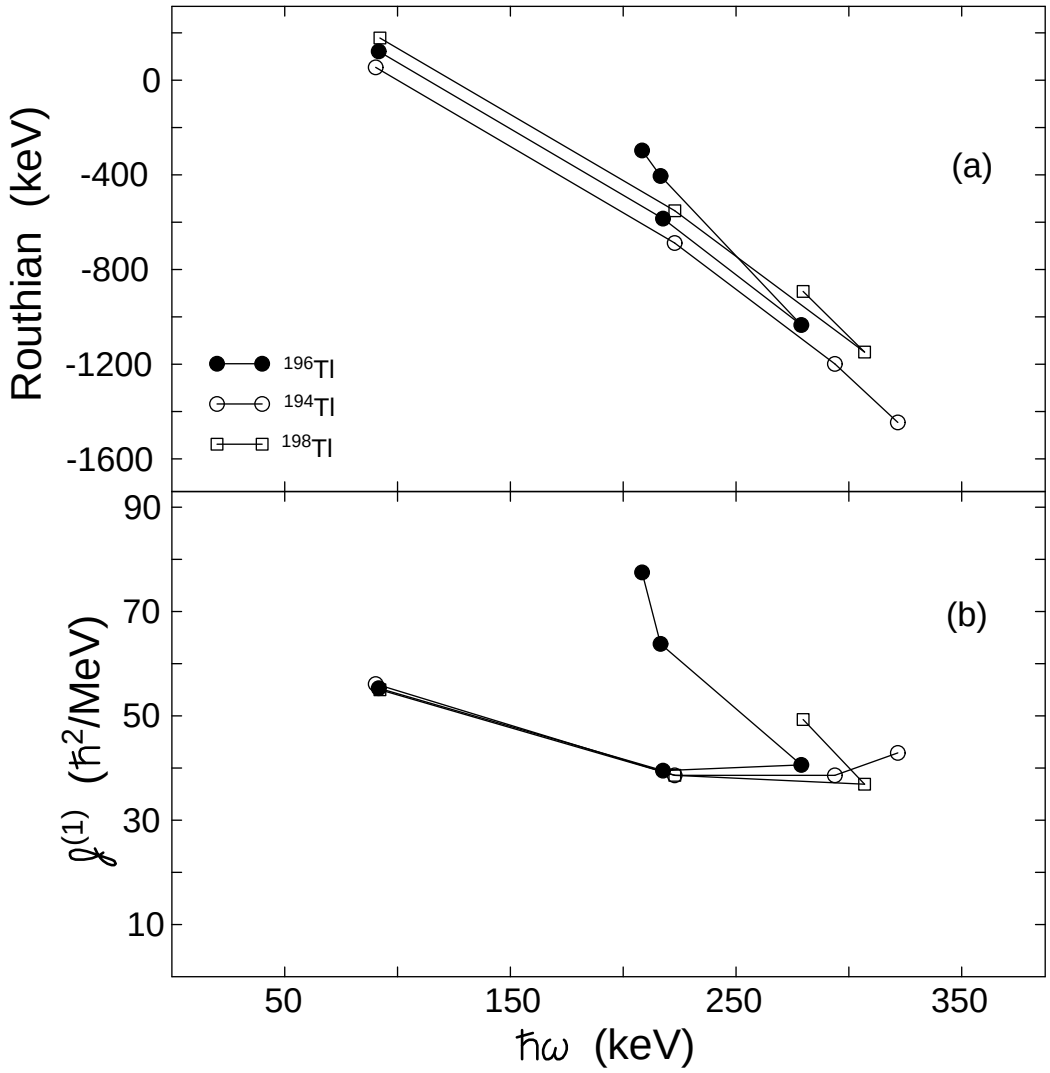

Figure 6.3: Experimental Routhians pannel (a) and kinematic moment of inertia panel (b) extracted from Band 1 in ^{196}Tl compared to the corresponding bands in ^{194}Tl and ^{198}Tl as a function of rotational frequency. The Harris parameters $\mathscr{I}_0 = 8\ \hbar^2/\mathrm{MeV}$ and $\mathscr{I}_1 = 40\ \hbar^4/\mathrm{MeV}^3$ were used.

developed in the figure and therefore we can not predict the bandcrossing frequencies of these nuclei. At the bandcrossing frequency, the Coriolis force is strong enough to break up a pair of neutrons and align the individual angular momentum of each nucleon along the rotation axis.

6.4 Alignments, kinematic moments of inertia and Routhians for Band 2 and 3

The Routhians, alignment, and kinematic moment of inertia for Band 1, 2 and 3 are plotted in Figure 6.4 panel (a), (b) and (c) respectively. Panel (a) shows that Band 2 is at excitation energy of about 1.5 MeV above Band 1 and Band 3. This energy is sufficient to break a pair of nucleons, and therefore Band 2 is likely to be associated with a 4-quasiparticle configuration. The alignment for this band (plotted in panel (b)) shows that Band 2 is slightly at higher alignment than Band 1 which implies that Band 2 may involve either high-j or low-Ω quasiparticles which contribute more to the alignment. The kinematic moment of inertia for this band plotted in panel (c), shows that Band 1 and Band 2 have about the same moment of inertia and therefore might have similar deformations.

Panel (a) of Figure 6.4 shows that the Routhians of Band 1 lie very close in energy to those of Band 3. This suggests that Band 3 is also a 2-quasiparticle band like Band 1. In panel (b) it can be seen that Band 3 has lower alignment with respect to Band 1 which indicates that Band 3 may involve one or both quasiparticles of higher Ω than in Band 1. In panel (c) one can see that the kinematic moment of inertia for Band 3 have lower values compared to Band 1. This indicates that Band 3 is likely to have different features from Band 1 including pairing, deformation, particle angular momentum etc.

Band 2 and 3 show to have different configurations than Band 1 as discussed above, these configurations however could not be determined from the $B(M1)/B(E2)$ method

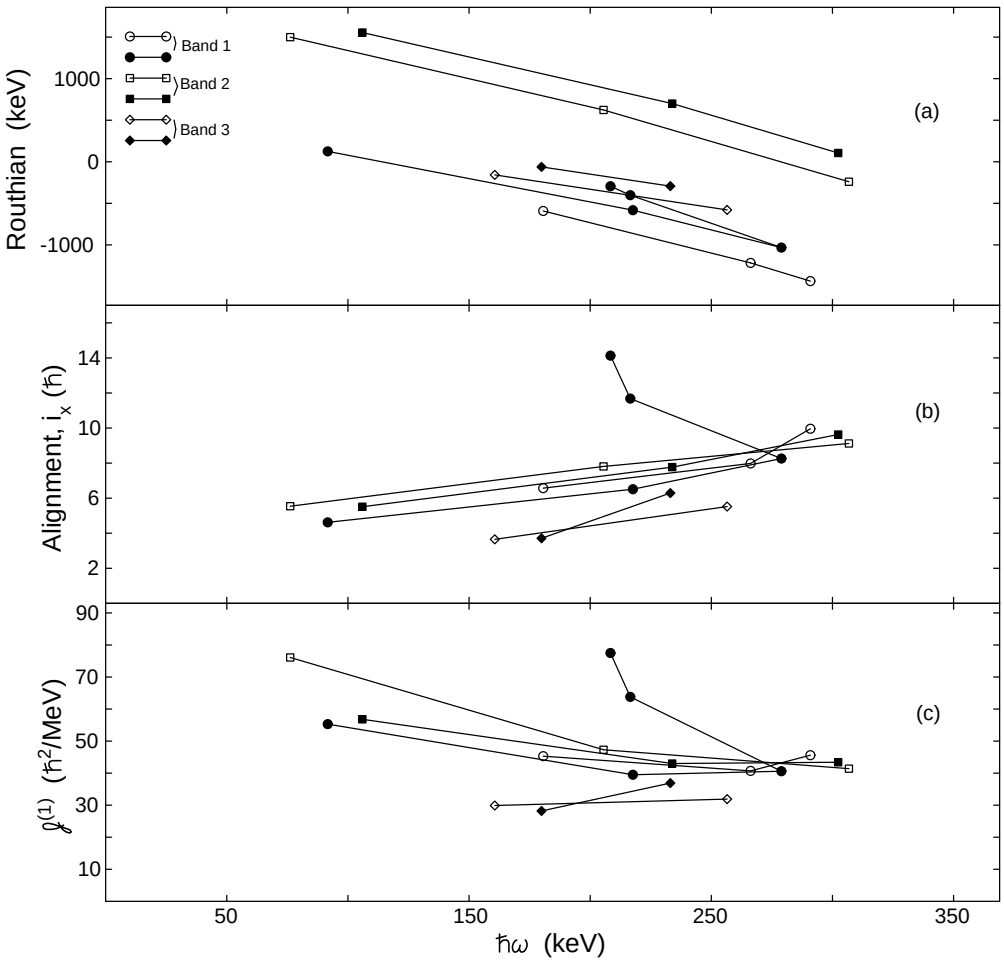

Figure 6.4: Panel (a),(b) and (c) show the experimental Routhians, alignment and kinematic moment of inertia respectively for Band 1, 2 and 3 in ^{196}Tl. The open (closed) symbols represent the signature $\alpha = 0$ (1). The Harris parameters $\mathscr{I}_0 = 8\ \hbar^2/\mathrm{MeV}$ and $\mathscr{I}_1 = 40\ \hbar^4/\mathrm{MeV}^3$ were used.

because there was a lack of data needed for theoretical calculations such as quadrupole moments, quadrupole deformation parameters and g-factors for Band 2 and 3 which may be obtained from lifetime measurements. Thus, Band 2 and 3 could not be assigned the configurations.

6.5 Total Routhian surface calculations for Band 1

The TRS calculations for the 2-quasiparticle $\pi\, h_{9/2} \otimes \nu\, i_{13/2}$ in ^{194,196,198}Tl were calculated by H. Pai *et al.* [1] as a function of β_2 and γ deformations, at rotational frequency of $\hbar\,\omega = 0.11$ MeV using the Hartee-Fock-Bogoliubov code of Nazarewicz *et al.* described in Ref. [26]. The contour plots are shown in Figure 6.5 panel (a), (b) and (c) for for Band 1 in ^{196}Tl, ^{194}Tl and ^{198}Tl respectively. One can see that the plots predict the minima in the potential energy (deformation favoured by the nucleus) at $\beta_2 \sim 0.12$ and $\gamma \sim$ - 57° consistent with an oblate deformation. These deformation parameters were used to calculate the theoretical $B(M1)/B(E2)$ values for the purpose of determining the nuclear configuration of Band 1 in ^{196}Tl. It is clear that Band 1 in ^{194,196,198}Tl have very similar deformations and they may therefore share a similar structure.

6.6 Summary and conclusion

This work presents the study of high-spin states in ^{196}Tl via the ^{197}Au(He,5n)^{196}Tl nuclear reaction at a beam energy of 63 MeV. The ground-state band, Band 1, was assigned the configuration of $\pi h_{9/2} \otimes \nu i_{13/2}$ from the measured and calculated $B(M1)/(E2)$ ratios. Band 2 and 3 could not be discussed in depth because the deformation parameters and g-factors needed for calculations were not available in the literature. These could be determined from lifetime measurements.

One of the objectives of the present study was to assign the spins and parities to the levels and to search for chiral bands in this nucleus. The occurrence of chirality will provide

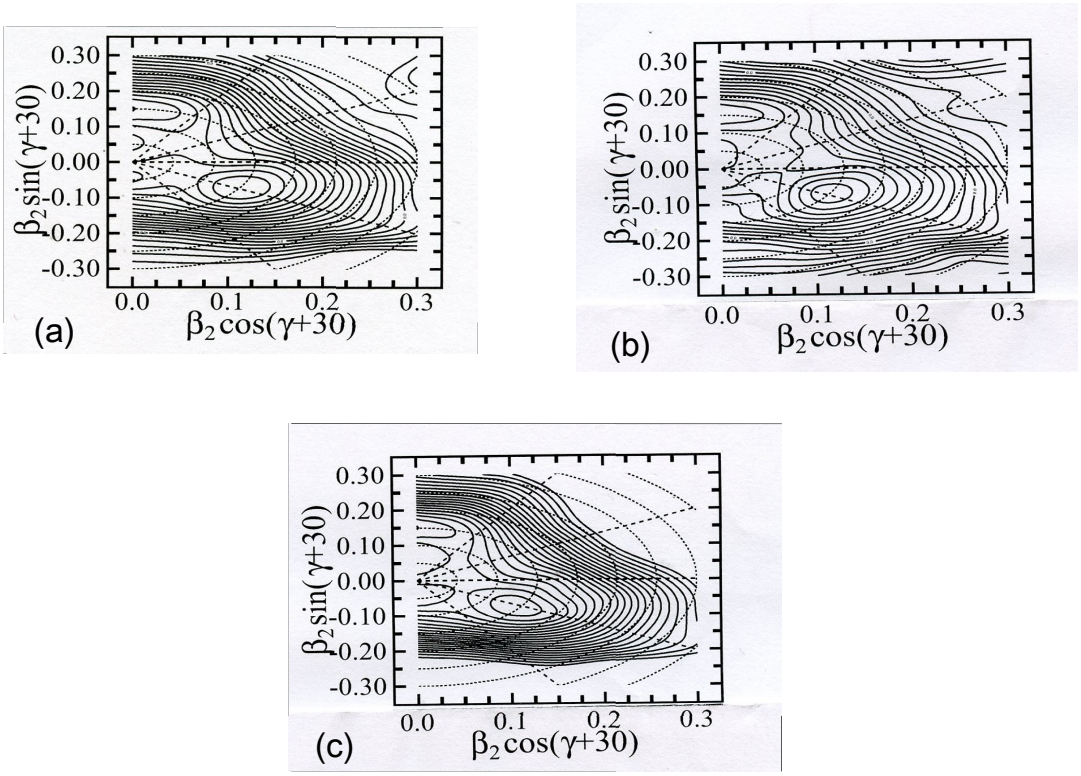

Figure 6.5: Calculated total Routhian surfaces for Band 1 in ^{196}Tl (panel (a)) compared to the corresponding bands in ^{194}Tl (panel (b)) and ^{198}Tl (panel (c)) at $\hbar\,\omega$=0.11 MeV. The energy difference between contours is 400 keV [1].

a unique test for the existence of stable triaxial nuclear shapes at moderate spins [28].

The results of our work shows no evidence of the presence of chiral bands in the ^{196}Tl nucleus since no partner bands were observed in our data. It should be noted that based on the fact that two 2-quasiparticle bands associated with chiral symmetry were observed in ^{198}Tl by E. Lawrie *et al.* [15] and that two 4-quasiparticle bands in ^{194}Tl were interpreted as possible chiral bands by P. Masiteng *et al.* [16] it is likely that chiral bands could also be present in ^{196}Tl as many properties of these nuclei are very similar. Further studies with increased statistics in ^{196}Tl might reveal such bands.

To meaningfully describe the rotational behaviour of the ^{196}Tl nucleus, further studies should focus on Cranked Shell Model calculations in order to understand the physical properties of the bands. Lifetime measurements and TRS calculations are also needed in order to determine the shapes and configurations of Band 2 and 3.

Bibliography

[1] H. Pai *et al. Nucl. Phys.*, arXiv:1201.6596v2, (2012).

[2] H. Pai *et al. Nucl. Phys.*, arXiv:1307.2056v1, (2013).

[3] C. Y. Xie *et al. Phys. Rev.*, **C 72**:044302, (2005).

[4] N. Nenoff *et al. Nucl. Phys.*, **A 629**:621, (1998).

[5] D. Mehta *et al. Nucl. Phys.*, **A 339**:317–323, (1991).

[6] S. Juutinen *et al. Nucl. Phys.*, **A 526**:346, (1991).

[7] A. J. Kreiner *et al. Nucl. Phys.*, **A 308**:147–160, (1978).

[8] A. J. Kreiner *et al. Phys. Rev.*, **C 47**:24, (1981).

[9] A. J. Kreiner *et al. Phys. Rev.*, **C 23**:2, (1981).

[10] A. J. Kreiner *et al. Phys. Rev.*, **C 22**:6, (1980).

[11] A. J. Kreiner *et al. Nucl. Phys.*, **A 282**:243–268, (1977).

[12] A. J. Kreiner *et al. Phys. Rev.*, **C 21**:3, (1980).

[13] R. M. Lieder *et al. Nucl. Phys.*, **A 299**:255, (1978).

[14] H. L. Yadav *et al. Phys. Rev.*, **C 287**:121–122, (1978).

[15] E. A. Lawrie *et al. Phys. Rev.*, **C 78**:021305(R), (2008).

[16] P. L. Masiteng *et al. Phys. Lett.*, **B 719**:83–88, (2013).

[17] K. S. Krane. *Introductory Nuclear Physics*. John Wiley and Sons, New York, (1988).

[18] E. S. Paul. *NSG Postgraduate Lectures*. University of Liverpool, (2010).

[19] N. Alkhomashi. *Beta Decay Studies of Heavy Neutron-Rich Nuclei Around A = 190*. PhD thesis, University of Surrey, (2010).

[20] R. F. Casten. *Exotic Nuclear Structure from a Simple Perspective*. Oxford University Press Inc., New York, (2001).

[21] E. A. Lawrie and D. G. Roux. *Nuclear Physics Honours Notes*. University of Western Cape, (2012).

[22] D. R. Bengtsson and S. Faunendorf. *Nucl. Phys.*, **A 327**:139, (1979).

[23] F. Stephens. *Rev. Mod. Phys.*, **A 47**:43, (1975).

[24] W. Nazarewicz *et al. Nucl. Phys.*, **A 512**:61, (1990).

[25] Mukherjee *et al. Nucl. Phys.*, **A 829**:137, (2009).

[26] W. Nazarewicz *et al. Nucl. Phys.*, **A 435**:397, (1985).

[27] S. Frauendorf and J. Meng. *Nucl. Phys.*, **A 617**:131, (1997).

[28] S. C. Pancholi. *Exotic Nuclear Excitations*. Springer, (2011).

[29] O. Shirinda and E.A. Lawrie. *Eur. Phys. J.*, **A 48**:118, (2012).

[30] `http://www.cns.s.u-tokyo.ac.jp/nuspeq/index.php?Glossary%2FFusionReaction`, Dec 2013.

[31] M. Blann *et al. Nucl. Inst. and Meth.*, **B 265**:490–494, (1988).

[32] A. Görgen. *Gamma-Ray Spectroscopy*. Lectures presented at IOP Nuclear Summer School, UK, (2005).

[33] G. Knoll. *Radiation Detection and Measurement*. John Wiley and Sons, (2000).

[34] J. L. Easton. New band in ^{192}Tl using gamma spectroscopy techniques. Master's thesis, University of Western Cape, (2011).

[35] G. Nelson and D. Reilly. *Phys. Rev.*, **C 732**:333, (1991).

[36] iThemba LABS. Afrodite array operating procedure. (2005).

[37] `http://www.canberra.com/products/detectors/germanium-detectors.asp`, Dec 2013.

[38] P. J. Nolan *et al. Annual. Rev. Nucl. Part. Sci*, **A 45**:516–607, (1994).

[39] P. T. Greenless. PhD thesis, University of Liverpool, (1999).

[40] T. M. Ramashidza. Gamma spectroscopy of the doubly-odd ^{194}Tl nucleus. Master's thesis, University of Western Cape, (2006).

[41] `http://www.midas.triumf.ca`, Feb 2014.

[42] `http://lise.nscl.msu.edu/pace4.html`, Feb 2014.

[43] G. Gilmore and J. Hemingway. *Practical Gamma-ray spectrometry*. John Wiley and Sons; New York, (1995).

[44] D. C. Radford. *Phys. Rev.*, **A 308**:297, (1995).

[45] D. C. Radford. *Nucl. Instr. and Meth.*, **A 361**:297, (1995).

[46] A. E. Stuchbery and M. P. Robinson. *Phys. Rev.*, **C 485**:753, (2002).

[47] N. Schunck *et al. Acta Phys. Pol.*, **B 36**:1071, (2005).

[48] C. Droste *et al. Nucl. Instr. and Meth.*, **A 378**:518, (1996).

[49] Z. Chunmei. *Nuclear Data Sheets*, **A 83**:145, (1998).

[50] T. Morinaga and T. Yamazaki. *In-Beam Gamma-Ray Spectroscopy.* North - Holland Publishing Company, (1976).

[51] F. Donau *et al. Nucl. Phys.*, **A 471**:469, (1987).

[52] R. Kroth *et al. Phys. Lett.*, **97B**:198, (1980).

[53] M. Guttormsen *et al. Nucl. Phys.*, **A 312**:155, (1983).